iScience

CellPress

Article

Self-Assembled Porous-Silica within N-Doped Carbon Nanofibers as Ultra-flexible Anodes for Soft Lithium Batteries

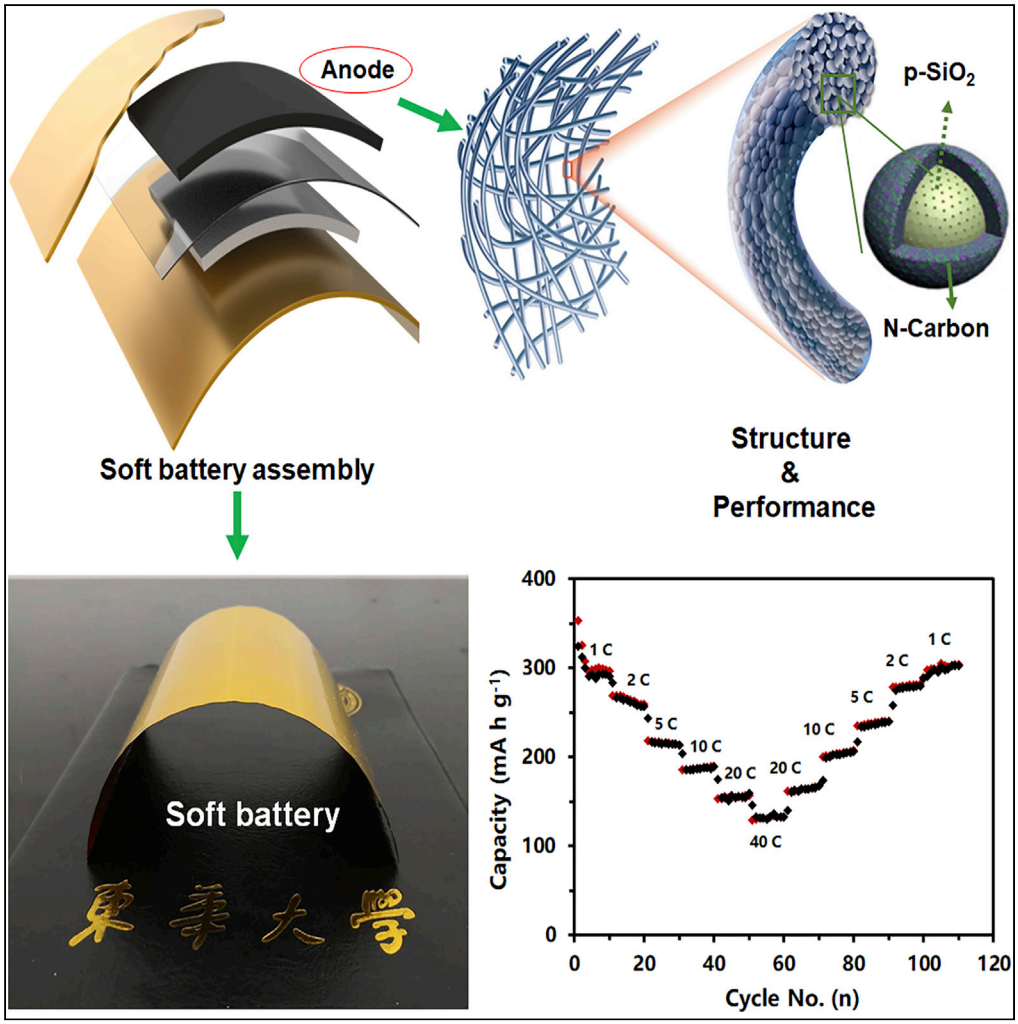

Ahmed A. Aboalhassan, Jianhua Yan, Yun Zhao, Keqi Dong, Xiao Wang, Jianyong Yu, Bin Ding

yanjianhua@dhu.edu.cn (J.Y.)
binding@dhu.edu.cn (B.D.)

HIGHLIGHTS

A scalable method is developed for the fabrication of flexible silica anodes

The flexible mechanisms of carbon nanofiber and silica films are illustrated

High-silica-loading anodes exhibit long cycle stability and high rate capability

Soft silica anodes show appealing properties for soft batteries

Aboalhassan et al., iScience *16*, 122–132
June 28, 2019
https://doi.org/10.1016/j.isci.2019.05.023

iScience

CellPress

Article

Self-Assembled Porous-Silica within N-Doped Carbon Nanofibers as Ultra-flexible Anodes for Soft Lithium Batteries

Ahmed A. Aboalhassan,[1,2] Jianhua Yan,[1,3,*] Yun Zhao,[1] Keqi Dong,[1] Xiao Wang,[2] Jianyong Yu,[3] and Bin Ding[3,4,*]

SUMMARY

Silica is an attractive anode material for soft lithium batteries owing to its high specific capacity, but it suffers severe problems of large volume change and unstable solid-electrolyte interface. Moreover, it is a challenge to fabricate flexible silica anodes. Here, we report a low-cost and scalable strategy to create flexible anodes of N-doped carbon nanofiber-confined porous silica (p-SiO_2@N-CNF) by developing a sol-gel electrospinning process followed by carbonization. This approach causes the p-SiO_2 nanoparticles (NPs) to be self-assembled within the N-CNFs, which act like elastomer and electrolyte barrier to accommodate volume changes and to enhance the stability of SiO_2, whereas the NPs act as soft plasticizer providing strength to the CNF skeletons. Benefiting from the hierarchical structures, the anodes with high p-SiO_2 loadings (>1.6 mg/cm^2) exhibit exceptional cycling performance (>1,000 cycles) in terms of bending, current rate, and capacity. Moreover, the batteries remain stable when discharging at 0.5 C and charging at 2 C.

INTRODUCTION

The evolving soft electronics and portable electronics require soft, lightweight, and durable lithium (Li)-ion batteries (LIBs) as power sources (Etacheri et al., 2011; Goodenough and Kim, 2009; Hu and Sun, 2014; Rao et al., 2018; Wang et al., 2017; Winter et al., 2018; Yue et al., 2016). SiO_2 has been highlighted as a promising anode material owing to its large specific capacity as part of the development of high-energy-density LIBs (Chang et al., 2012; Goriparti et al., 2014; Manthiram, 2011). Although the huge volume changes of SiO_2 and the side reactions with the electrolytes during cycling were identified as the main reasons of short cycle lives of SiO_2 anodes (Beaulieu et al., 2001; Obrovac and Christensen, 2004; Obrovac et al., 2007), it has been recently recognized that nanoscale designs contributed substantially to improve the cycle lives (Li et al., 2012; Meng et al., 2015; Wu et al., 2012; Yang et al., 2014; Yuan et al., 2016).

However, achieving long-term stability still remains challenging for the nanoscale anodes with commercial level of SiO_2 loadings (e.g., >1 mg/cm^2). For one thing, SiO_2 nanoparticles (NPs) were susceptible to separate from the conductive additives during the huge volume changes, which easily led to structural degradation and unstable solid-electrolyte interface (SEI) (Aricò et al., 2005; Sasidharan et al., 2011; Tu et al., 2014; Yan et al., 2013). For another, SiO_2 was commonly known to be an intrinsic electronically insulating material owing to its wide band gap (Sun et al., 2008). Although coating SiO_2 with carbon materials was a solution to such problems, the capacities of the LIBs that contained high SiO_2 loading anodes also fade quickly (An et al., 2017; Kim et al., 2014). In addition, from a practical perspective, it is still a great challenge to manufacture large-scale flexible electrodes with low resistances by using the available thin-film technologies. The conventional SiO_2 anodes utilizing binders and metal current collectors were typically too rigid and heavy, and therefore could not meet the requirements of soft battery applications (Dirican et al., 2015; Jang et al., 2009; Zhou et al., 2012).

Here, we propose a scalable strategy of manufacturing hierarchical structured anodes with commercial level of SiO_2 loadings and durable flexibility to tackle the aforementioned problems. Having noticed that the SEI stability and stress dissipation during the volume expansion of SiO_2 are key to the robust operation of SiO_2 anodes (Chen et al., 2017), porous SiO_2 (p-SiO_2) NPs were first synthesized via a sol-gel technique by employing the positively charged cetyltrimethyl ammonium bromide (CTAB) as a soft template (Figure 1A) (Wang et al., 2016a). We did not wash the residual CTAB off after the reactions because a small amount of CTAB made these p-SiO_2 NPs easier to be dispersed in the spinning solutions. The p-SiO_2 NPs shared the characteristics of limited volume changes of nanoscaled SiO_2 and sufficient

[1]Key Laboratory of Textile Science & Technology, Ministry of Education, Donghua University, Shanghai 201620, China

[2]State Key Laboratory for Modification of Chemical Fibers and Polymer Materials, College of Materials Science and Engineering, Donghua University, Shanghai 201620, China

[3]Innovation Center for Textile Science and Technology, Donghua University, Shanghai 200051, China

[4]Lead Contact

*Correspondence: yanjianhua@dhu.edu.cn (J.Y.), binding@dhu.edu.cn (B.D.)

https://doi.org/10.1016/j.isci.2019.05.023

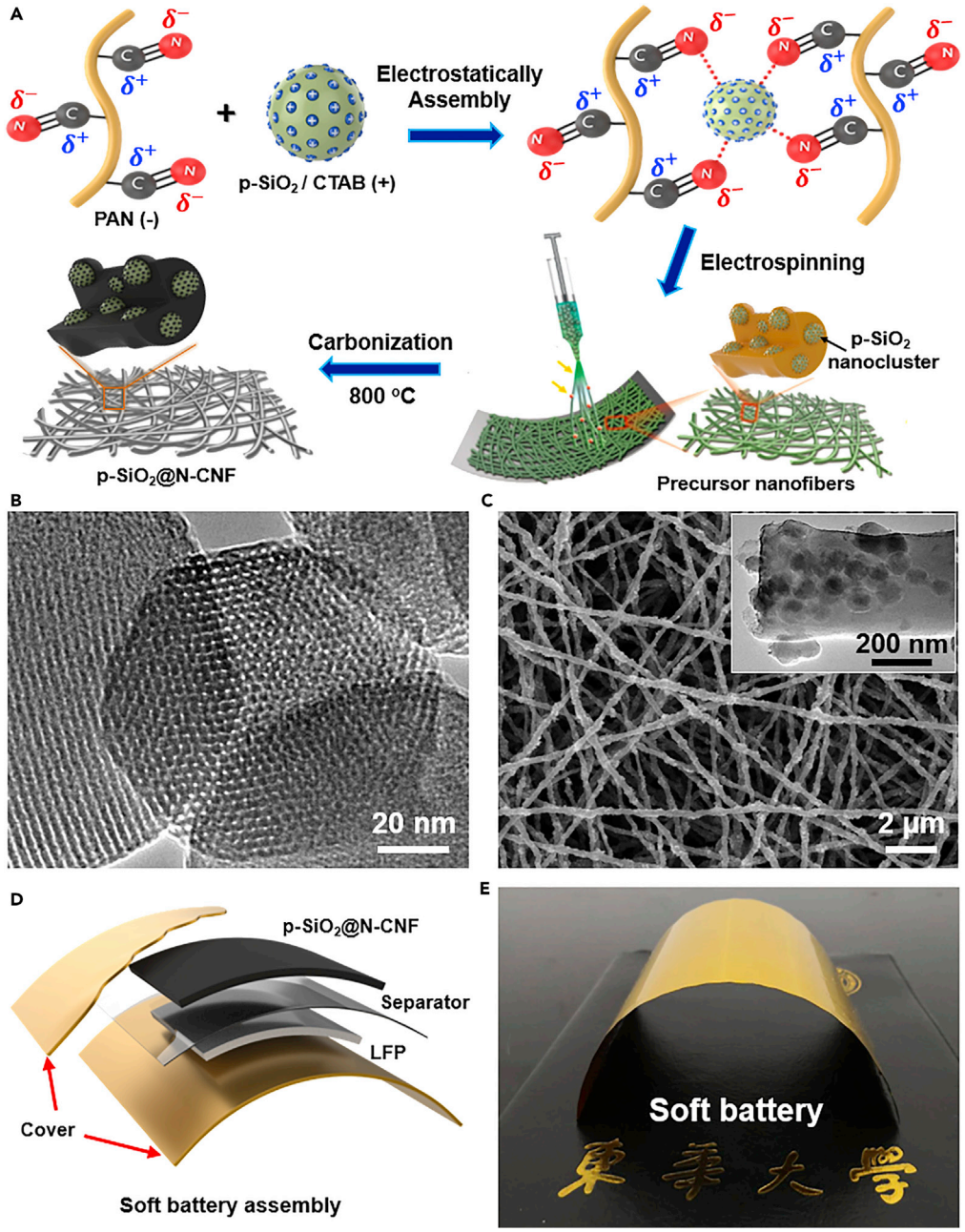

Figure 1. Fabrication of the Ultra-flexible Anodes of p-SiO_2@N-CNF and Their Applications in Soft LIBs

(A) Schematic illustration for the electrostatic assembly of p-SiO_2 NPs containing CTAB with PAN followed by electrospinning and carbonization to fabricate flexible p-SiO_2@N-CNF anode.

(B) TEM image of the honeycomb-structured p-SiO_2 NPs.

(C) An SEM image of the nanofibrous film of p-SiO_2@N-CNF with interconnected architectures. The inset figure is a single CNF that contained overlapped p-SiO_2 nanoclusters.

(D) The inner structures of typical soft Li-batteries that contained the flexible p-SiO_2@N-CNF anode and $LiFePO_4$ (LFP) cathode.

(E) The digital image of the soft Li-battery.

porosity for SiO_2 volume expansions (An et al., 2017). Then a sol-gel electrospinning technique was developed to assemble these NPs into polyacrylonitrile (PAN) precursor nanofibers (NFs). This strategy allowed the positively charged p-SiO_2-CTAB composites to electrostatically attract the negatively charged PAN in

the spinning solution as shown in Figure 1A, which led to uniformly distributed p-SiO_2 nanoclusters within the matrix of PAN NFs. During the subsequent calcination process, the CTAB was decomposed and the PAN was converted into N-doped carbon nanofibers (N-CNFs), consequently forming overlapped p-SiO_2 nanoclusters within N-CNFs (Sui et al., 2016; Ye et al., 2017).

The advantages of this reported material design lie in the following three levels. (1) The core-shell structured p-SiO_2 nanoclusters decreased the exposed specific surface areas of p-SiO_2 and thus stabilized the SEI. (2) The porous and nanoscale SiO_2 structures alleviated the volume changes and reduced pulverization of SiO_2, whereas the 1D CNFs had a minimum transverse volume expansion effect (Ji et al., 2019; Li et al., 2018; Qu et al., 2018). (3) The ultra-flexible electrospun N-CNFs, serving as the anode skeleton, could continuously and efficiently transport e^- and Li^+ to the non-conductive p-SiO_2 nanoclusters, which in turn acted as a soft plasticizer providing strength to the N-CNFs (Ge et al., 2016; Hu et al., 2013; Li et al., 2017). With all these merits together, the anodes with commercial level of SiO_2 loadings (>1.6 mg/cm^2) exhibited high cycling performance in terms of current rates (0.1–40 C), capacity retention (0.038% fade per cycle over 500 cycles at 0.1 C and 0.026% fade per cycle over 1,000 cycles at 1 C), and Coulombic efficiency (CE) (>97% all the way). Moreover, soft batteries containing such flexible anodes displayed stable cycling performance under various bending angles and could be stable over 700 cycles when discharging at 0.5 C and charging at 2 C.

RESULTS AND DISCUSSION

Electrode Characterizations

The p-SiO_2 NPs had honeycomb structures in which the ordered hexagonal pores with an average pore size of 4 nm were aligned in straight channels, as clearly viewed in Figure 1B. These porous NPs had a uniform morphology with an average diameter of 108 nm (Figure S1 correlated to the particles size of mesoporous silica in Figure 1B) and a pore volume of 0.87 cm^3/g (Figure S2 and Table S1 illustrate the surface area and the pore size distribution of the free p-SiO_2 NPs and loaded on N-CNFs and related to the Brunauer–Emmett–Teller isotherm in Figure 2B). The anode of p-SiO_2@N-CNF had a SiO_2 content of 37.7 wt % (Figure S3 shows the loading ratio tested by thermogravimetric analysis), and the whole membrane could be bent from 0° to 180° without forming any cracks as viewed in the scanning electron microscopic (SEM) images (Figure S4). The NFs in the anode framework offered a high degree of interconnectivity with micrometer-sized pores in between (Figure 1C). The p-SiO_2 NPs in N-CNFs tended to aggregate and formed nanoclusters. Nevertheless, these p-SiO_2 nanoclusters were submerged within N-CNFs, as verified by transmission electron microscopy (TEM, inset of Figure 1C). Therefore the produced ultra-flexible membranes of p-SiO_2@N-CNF could be easily assembled into soft batteries as described in Figures 1D and 1E.

The surfaces of p-SiO_2 NPs were covered by a thin and compact layer of graphitic carbon (Figure 2A), as verified by the interplanar distance of ≈0.41 nm, which matched well with the d-spacing of (002) in graphitic carbon (Liu et al., 2013). This advanced hierarchical structure significantly decreased the exposed surface areas of p-SiO_2 NPs from 1,090 m^2/g to 80.78 m^2/g (p-SiO_2@N-CNF), which was even much smaller than 256 m^2/g of the pure N-CNF (Figure 2B). Of note, the carbonization process created randomly distributed graphitic and amorphous carbon domains inside the CNFs that possessed a multicrystalline structure, as verified by X-ray diffraction (Figure 2C). The p-SiO_2 NPs demonstrated a broad diffraction peak at 24°, corresponding to amorphous SiO_2 (Aricò et al., 2005). Although both pure CNFs and p-SiO_2@N-CNF displayed two broad peaks at 24° and 43°, respectively, that were analogous to the diffraction planes of (002) and (100) in graphitic carbon (Wang et al., 2016b), p-SiO_2@N-CNF had a higher degree of crystalline at (100) plane than pure N-CNFs. To further explore the graphitization degrees, Raman scattering was tested for both samples (Figure 2D). The D-band (1,345 cm^{-1}) and G-band (1,580 cm^{-1}) in both samples represented the disordered amorphous carbon and ordered graphitic sp^2 hybridization carbon, respectively. The disordered degree of p-SiO_2@N-CNF was 1.04 (calculated by the ratio of peaks' intensities, $R_D = I_D/I_G$), which was slightly higher than 1.02 of the pure CNFs.

A typical single fiber was examined by energy-dispersive spectrometry, which revealed a uniform distribution of Si, O, and N within the C matrix (Figure 2E). The N originated from the adopted precursor materials of PAN, which had the ability of *in situ* heteroatom doping within the carbonous structure via cyclization mechanism (Pan et al., 2015; Tan et al., 2017). For intensely investigating the functional

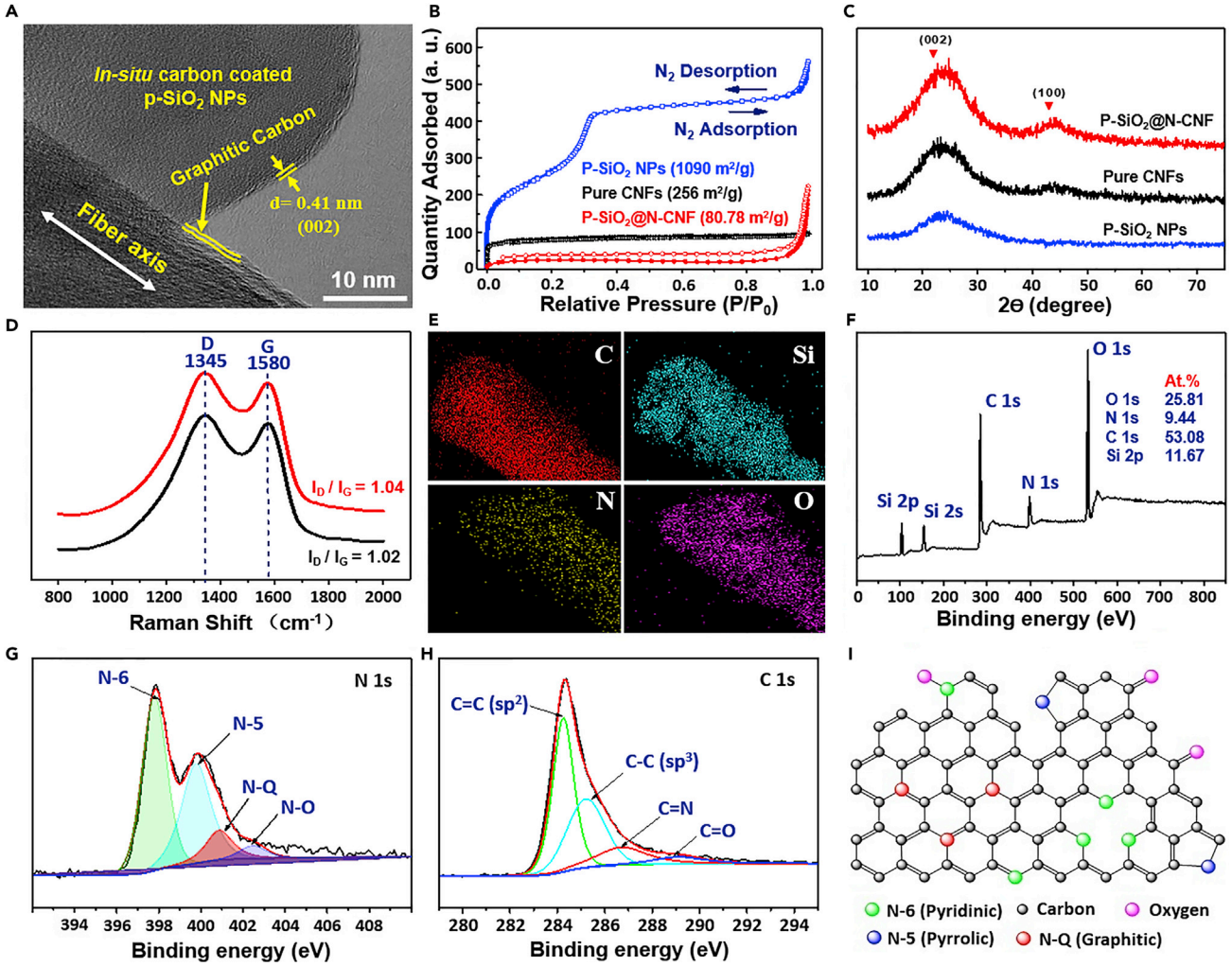

Figure 2. Characterizations of the Anodes of p-SiO_2@N-CNF

(A) TEM image to show *in situ* graphitic and amorphous carbon coatings over p-SiO_2 NPs.

(B) N_2 adsorption-desorption isotherms of p-SiO_2 NPs, pure N-CNFs, and p-SiO_2@N-CNF.

(C) XRD diffractograms of p-SiO_2 NPs, pure N-CNFs, and p-SiO_2@N-CNF.

(D) Raman spectra of pure N-CNFs and p-SiO_2@N-CNFs.

(E) Energy-dispersive spectrometry mapping spectrum of p-SiO_2@N-CNF.

(F) XPS spectrum of p-SiO_2@N-CNF.

(G and H) High-resolution of (G) N 1s and (H) C 1s spectra of p-SiO_2@N-CNF.

(I) The proposed chemical model of N-doped carbon.

groups and their compositions, X-ray photoelectron spectroscopy (XPS) was performed as shown in Figure 2F. XPS displayed the presence of C 1s, O 1s, and N 1s, which matched well with the elemental mapping. Remarkably, the p-SiO_2@N-CNF had a high N-content (atomic ratio of 9.44%) and the atomic ratio of Si and O was around 1:2. The N-doping was favorable for boosting the electronic conductivity of carbon (Tan et al., 2017). Moreover, the deconvolution of N 1s (Figure 2G) displayed four characteristic peaks at 397.2, 399.7, 400.88, and 402.48 eV equivalent to the four N groups N-6, N-5, N-Q, and N-Ox, respectively. These groups were transformed from PAN, through which pyridinic, pyrrolic, and graphitic N were formed (Wu et al., 2018). Specially, the N-Ox in N-CNFs could enhance electrolyte uptakes (Deng et al., 2016). Furthermore, four typical peaks at 284.3, 285.2, 286.7, and 289.4 eV were identified for C 1s, corresponding to sp^2 graphitic carbon, sp^3 hybridized carbon, C=N bond, and carbonyl groups, respectively (Figure 2H) (Panomsuwan et al., 2015). A proposed chemical model of these N groups in the carbon domains was sketched in Figure 2I. The presence of such doping

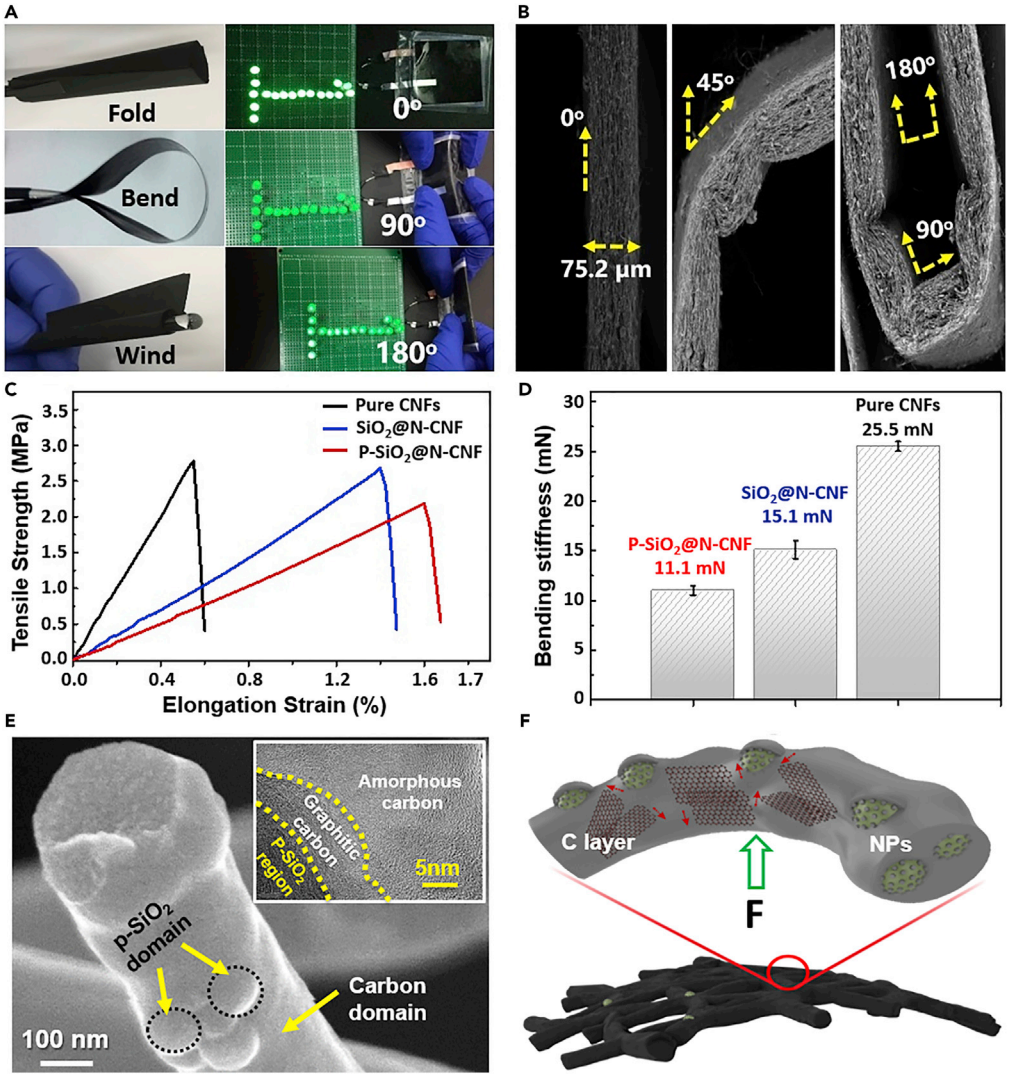

Figure 3. Mechanical Performance of the Anodes of p-SiO_2@N-CNF

(A) Digital photographs of the anode under various folding, winding, and bending states, and the photographs of using a soft $LiFePO_4$/p-SiO_2@N-CNF battery under different bending angles to light light-emitting diodes.

(B) SEM images of the flexible membrane in different bending angles.

(C and D) (C) Stress-strain curves and (D) Bending stiffness of pure CNFs, SiO_2@N-CNFs, and p-SiO_2@N-CNFs.

(E) Cross-sectional images of a single NF that show overlapped p-SiO_2 nanoclusters within the graphitic and amorphous carbon domains.

(F) Demonstrative 3D illustration of the integrated p-SiO_2 NPs in N-CNFs under a bending force.

groups in the CNF microstructure could enhance the electrochemical performance of electrodes (Wang et al., 2016a).

Mechanical Flexibility Investigations

The made-up anodes had intriguing shape memory performance and could maintain their original shapes without fragility on various deformations including folding, winding, and binding states (Figure 3A). Moreover, deeply exploring the cross-sectional view of the p-SiO_2@N-CNF showed that it had no cracks in the deformed membranes under diverse positions (Figure 3B). Dynamically, after removing the stress, the membrane could rapidly recover to its initial states automatically, and this step could be repeated for more than 1,000 times, demonstrating durable flexibility and robustness. When assembling the anode in a soft LIB, where $LiFePO_4$ (LFP) was used as cathode, it could work normally at different folding angles (Figure 3A).

To understand the flexibility, bending stiffness, and tensile stress-strain of pure CNFs, SiO_2@N-CNF, and p-SiO_2@N-CNF were measured. Here, as a control, we examined soft anodes of SiO_2@N-CNF, which were prepared by using commercial non-porous SiO_2 NPs with an average size of 100 nm. As shown in Figures 3C and 3D, p-SiO_2@N-CNF had the lowest stiffness of 11.1 mN and the largest elongation strains of 1.6%. The NF diameter had a great impact on the mechanical properties of these films. As shown in Figure S5, the average diameter of CNFs, SiO_2@N-CNF, and p-SiO_2@N-CNF were 265 $\pm$ 4, 305 $\pm$ 2, and 371 $\pm$ 2 nm, respectively. The increments in fiber diameters were closely related to the surface roughness of the p-SiO_2 NPs, and hence most of these p-SiO_2 nanoclusters are strongly overlapped within the CNFs as shown by the cross-sectional view of a single fiber from p-SiO_2@N-CNF (Figure 3E). In this design, the synthesized p-SiO_2 nanoclusters were covered by CTAB, as proved by Fourier transform infrared (FTIR) (Figure S6). With CTAB on surfaces, the p-SiO_2 NPs became positively charged and had the ability of self-interlocking with the negatively charged PAN chains in the spinning solution via electrostatic attraction. After pre-oxidizing the PAN precursor NFs, the CTAB was fully decomposed, as determined by the FTIR, in which the absorption peak at 2,922 cm^{-1} disappeared, indicating complete removal of the CTAB from the fabricated membrane. As a morphological comparison, the commercial non-porous SiO_2 NPs were allocated mostly out of the fibers as seen clearly in SEM (Figures S7A and S7B).

The high mechanical stability of p-SiO_2@N-CNF was ascribed to the advanced core-shell structure, in which the well-interlocked p-SiO_2 nanoclusters were submerged in both graphitic and amorphous carbon domains. The movements of the graphitic layers inside the N-CNFs facilitated the absorption of the applied force or scattering of force when bending the fiber via microscale movements (Figure 3F), and thus avoiding the NF breaking under a small external force. However, when a bigger external stress was applied to the pure CNFs without NP doping, the force would concentrate on one area and then initiate cracks, which spread rapidly all over the fibers without any blocking and finally led to fractures in the NFs. In the case of p-SiO_2@N-CNF, the applied force on the NF was faced by the interlocked p-SiO_2 NPs, which could scatter and level the concentrated stress. The rough and porous surfaces of the employed p-SiO_2 NPs made it easier to form well-interlocked composites of P-SiO_2/PAN polymers in the electrospinning solutions, which helped to form a perfect hierarchical CNF structure that contained uniformly distributed p-SiO_2 NPs. Therefore the p-SiO_2@N-CNF membrane showed the best mechanical flexibility as shown in Figure 3. This was proved by the high-resolution TEM image, which showed that the microstructural p-SiO_2 nanoclusters overlapped within both graphitic and amorphous carbon domains of N-CNF (Figures S7C and S7D).

Electrochemical Performance of the p-SiO_2@N-CNF Anodes

Cyclic performances of the Li/p-SiO_2@N-CNF and Li/N-CNF batteries were comparatively examined to determine the capacity contributions from p-SiO_2 NPs in the anode of p-SiO_2@N-CNF (Figure 4A). Both batteries demonstrated high CE and stable cycling performance at 0.1 C. However, the capacity of Li/p-SiO_2@N-CNF was much higher, i.e., 430 mA h/g versus 225 mA h/g over 120 cycles, corresponding to a capacity of 769 mA h/g contribution from the p-SiO_2 NPs.

The battery of Li/p-SiO_2@N-CNF exhibited typical charge/discharge profiles of combined CNFs and SiO_2 at 0.1 C (Figure 4B). The p-SiO_2@N-CNF anode had a voltage plateau shoulder from 0 to 1.5 V owing to a high voltage potential needed for Li^+ ions alloying-dealloying into SiO_2 (Guo et al., 2008). This result was verified by cyclic voltammetry (CV, Figure 4C), where there were two obviously separated anodic oxidation peaks at 0.31 and 0.46 V, corresponding to extraction of Li-ions from CNFs and SiO_2, respectively. In addition, from the first charge-discharge profile (Figure S8), there was a clear reduction peak at 0.55 V, which was associated with the formation of irreversible SEI and the possible irreversible reactions between Li ions and SiO_2 (Guo et al., 2008). Moreover, the two de-alloying oxidation peaks became sharp after the first cycle and the CV curves coincided well from the second to the 10th cycle, implying fast reaction kinetics and good electrochemical reversibility. Previous studies revealed that this increment in the de-alloying rate was caused by the formation of nano-Si phase embedded within the lithium oxide and lithium silicates after the first irreversible reactions, and the stable SEI originated from the shell carbons over SiO_2 NPs (Guo et al., 2008).

The batteries exhibited stable degrees of lithiation and de-lithiation with high CE around 100% at different current densities varying from 0.1–1 C (Figure 4D). For example, at 0.1 C, the discharge capacity slowly decreased from 507 to 410 mA h/g after 500 cycles, corresponding to a 0.038% capacity fade per cycle.

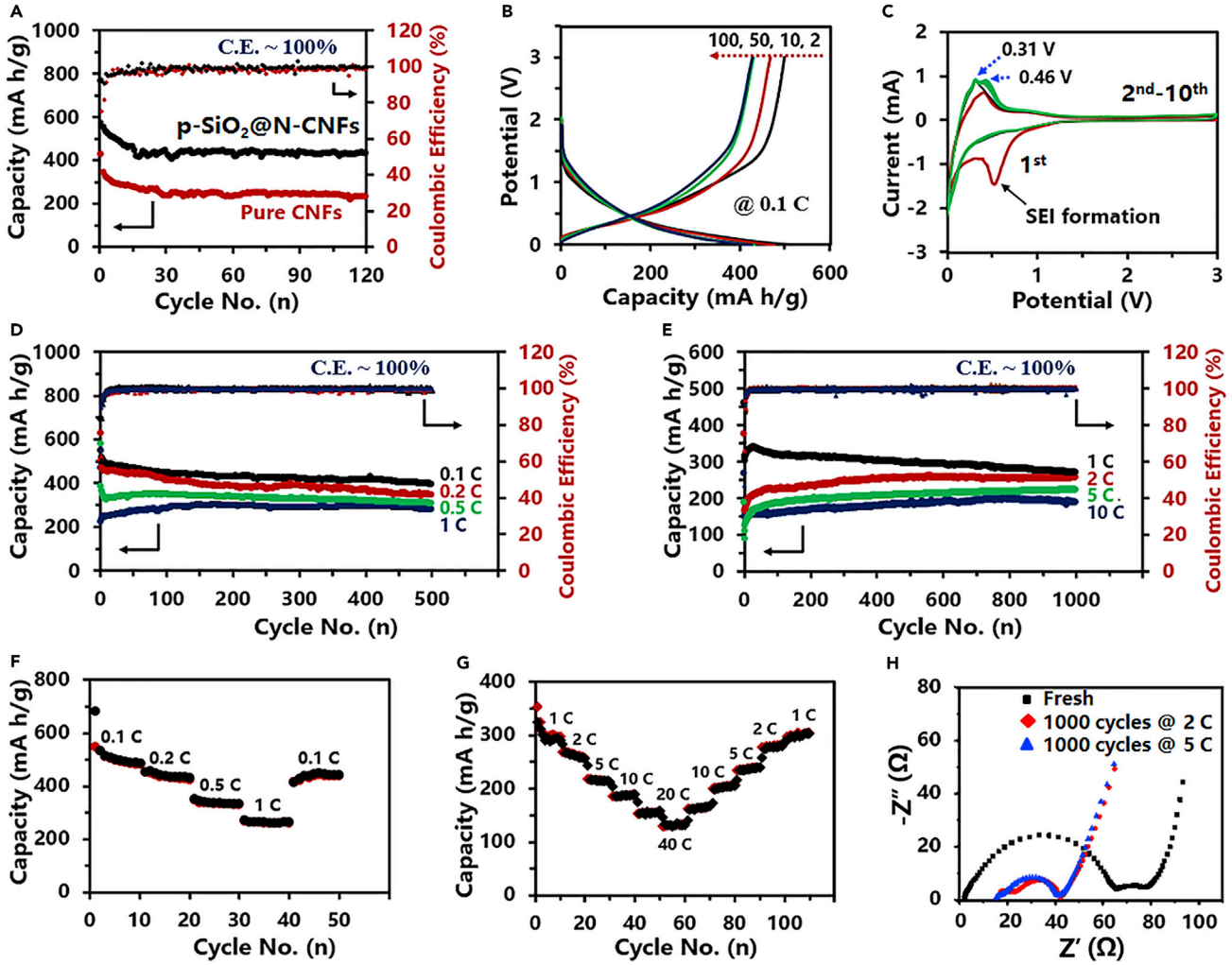

Figure 4. Battery Electrochemical Performance

(A) Comparison of cyclic performance of batteries containing the anodes of pure N-CNFs and p-SiO_2@N-CNFs.

(B) Galvanostatic charge-discharge profiles of the composite anodes from the second cycle to the 100th cycle at 0.1 C.

(C–E) (C) Continuous CV scans from the first to the 10th cycle of the composite anodes from 0 to 3 V at a scan rate of 0.1 mV/s. Long-term electrochemical tests of the batteries at (D) low current rates from 0.1 to 1 C and (E) high current rates from 1 to 10 C.

(F and G) Rate capabilities of batteries under (F) low current rates and (G) high current rates.

(H) Electrochemical impedance spectra of batteries at the fresh states and after the 1,000th cycle at 2 C and 5 C, respectively.

The reversible capacities of the other three batteries over 500 cycles were 340, 300, and 280 mA h/g at 0.2, 0.5, and 1 C, respectively. The stability of the batteries was further proved by testing them under high current rates of 1, 2, 5, and 10 C over 1,000 cycles (Figure 4E). Remarkably, the discharge capacity was fully recovered from 275 to 435 mA h/g when the currents were brought back from 1 C to the initial 0.1 C (Figure 4F). Of note, the returned capacity slightly increased when testing the batteries from 1 C to the very high current rate of 40 C (Figure 4G), indicating excellent rate capability of the anodes.

The unique anode structures of p-SiO_2@N-CNF promoted electrical conductivity and provided a shielding over p-SiO_2 NPs from continuous contact with the electrolytes, which improved the battery performance upon the repeated charge and discharge cycles. Figure 4H displays the Nyquist plots of a fresh battery and the cycled (1,000 cycles) battery at two different C rates (i.e., 2 C and 5 C). The fresh battery possessed low resistance compared with the cycled battery owing to the establishment of non-electronic conductive SEI layers, which were formed in the first cycle (Guo et al., 2008; Yuan et al., 2016). After 1,000 cycles at 2 C

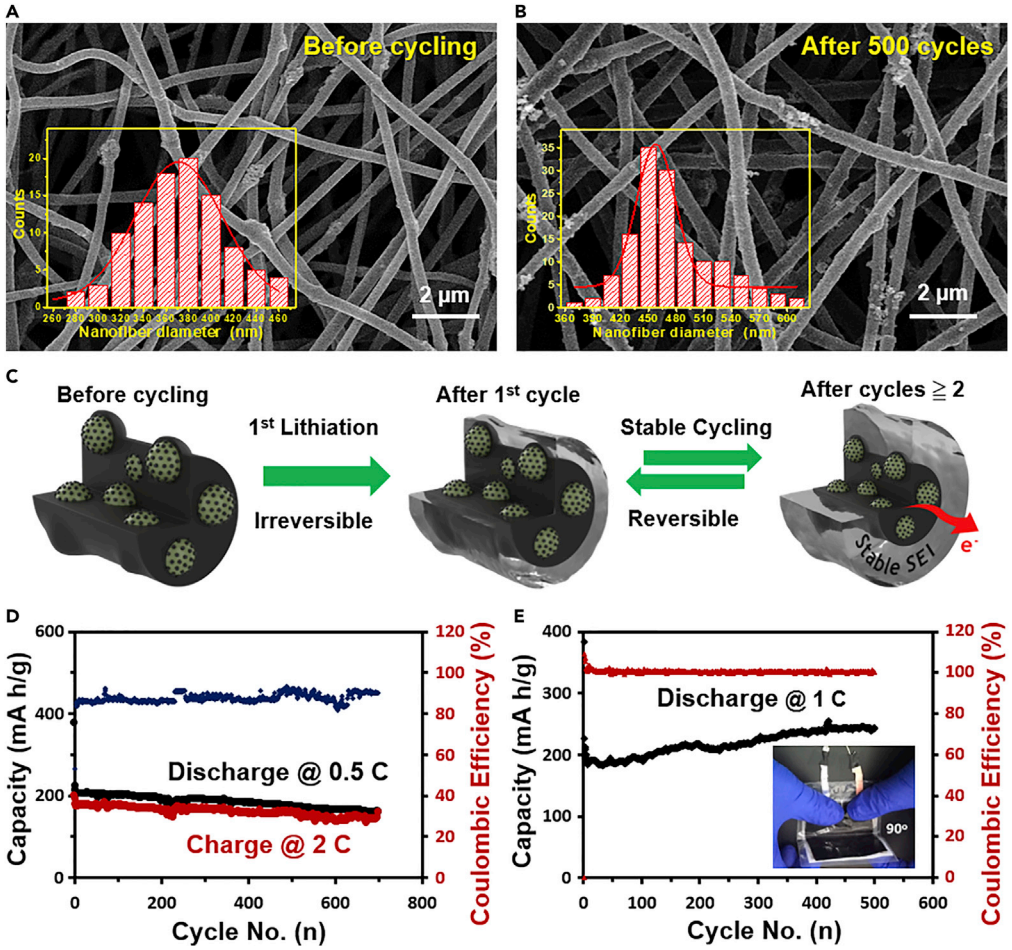

Figure 5. Postmortem Morphology, Stability Illustration, and Electrochemical Performance of the Bent Batteries

(A and B) SEM images of the composited anodes (A) before cycling and (B) after 500 cycles at 1 C. The inset figures are the corresponding nanofibers' diameter histograms.

(C–E) (C) Schematic illustration of the formation of stable SEI in the designed anodes. Cyclic performance of the soft Li-batteries (D) under a constant angle of 90° at 1 C and (E) at different rates for practical applications, i.e., a low discharge rate of 0.5 C and a high charge rate of 2 C.

and 5 C, the charge transfer resistances decreased a lot, suggesting the long-term SEI stability and fast Li-ion diffusion kinetics in the p-SiO_2@N-CNF anodes.

Postmortem Morphology Study and Performance of the Flexible p-SiO_2@N-CNF Anodes

The morphological changes after charge/discharge cycling are indicators to assess the battery stability performance. A comparative postmortem study of the NF morphology was investigated for a deeper understanding of the designed flexible anodes. Figures 5A and 5B display that the overlapped p-SiO_2 nanoclusters in the N-CNFs kept integrity with small transverse volume expansion after 500 cycles at 1 C. The NF diameter increased from 371 to 458 nm, corresponding to only 1.23 times of its initial value (inset of Figures 5A and 5B). As a comparison, after 500 cycles at 1 C, most of the NFs cracked in the anode of SiO_2@N-CNFs and the NF diameter increased from 305 to 529 nm, corresponding to 1.73 times volume change (Figure S9). Moreover, the anode containing 38 wt % p-SiO_2 NPs, 52 wt % CNFs, and 10 wt % polyvinylidene fluoride showed a much larger volume change and there were obviously cracks on the anode surface after 500 cycles at 1 C (Figure S10).

The cycling stability came from the stable SEI of the well-interlocked p-SiO_2 nanoclusters in the N-CNFs. Generally, SiO_2 irreversibly reacted with Li-ions in the first cycle and formed a matrix of lithium oxide and

lithium silicate (Guo et al., 2008). From the second cycle, the N-CNFs delivered e^- directly to the submerged p-SiO_2 NPs and therefore the battery could run normally with a stable SEI, as illustrated in Figure 5C. The SEI formation in the first cycle was attributed to the irreversible reaction between Li-ions and SiO_2 at 0.6 V (Figure S8). From the second cycle, a stable SEI was created over the anode. In contrast, the commercial SiO_2 nanoclusters had bad morphological stability after cycling (Figure S9). This clear stability of the designed nanostructure gave rise to high cyclic stability of the soft LIB (Li/p-SiO_2@N-CNF) under a constant degree of 90° as shown in Figure 5D. The bent battery delivered a reversible discharge capacity of 260 mA h/g at a discharge rate of 1 C over 500 cycles. At the same time, the battery demonstrated high stability with a CE of ~100%. In contrast, the battery (Li/SiO_2@N-CNF) with the commercial silica anode demonstrated rapid capacity fading and low CE (Figure S11). Considering that the daily-use batteries have a much higher charging rate than discharging rate, an experiment of our flexible anode was done under a high charging rate of 2 C while discharging at 0.5 C. Interestingly, the soft battery demonstrated reasonable stability (Figure 5E) and delivered a stable capacity of ~200 mA h/g for 700 cycles with a reasonable CE of ~90% and standard voltage profiles (Figure S12).

To the best of our knowledge, scalable fabrication technique to create anodes with an integration of durable mechanical flexibility and commercial level of SiO_2 loadings has not been reported previously. Using our laboratory equipment, we could easily obtain a big membrane with an area of 70 × 53 cm^2, as shown in Figure S13. The robust SiO_2 anode design methodology combined the advantages of stable SEI of core-shell structured p-SiO_2@C, continuous electrical conductivity of N-CNFs, and flexibility of the electrospun CNFs. It is worthy to note that during the lithiation process, the graphitic carbon acted as a belt that reserved the volume expansion spaces, whereas the amorphous carbon merged the p-SiO_2 NPs together without separations from the N-CNFs. In addition, the superior flexibility of the nanofibrous anodes guaranteed a smooth conductive channel during repeated cell operations under various bending forces and thus produced soft Li-batteries with long-term stability and high rate capability. The flexible anodes displayed better stability and durability (Figure S14) via a simple and feasible fabrication strategy compared with recently reported flexible lithium batteries (Chang et al., 2018; Jeschull et al., 2015; Kim et al., 2017). These findings will have a marked impact on the general approach for tailoring the properties of flexible p-SiO_2 anodes and show a high commercialization potential of the flexible anodes in constructing soft LIBs.

Conclusions

We have reported a flexible 1D N-CNF anode structure containing well-interlocked p-SiO_2 nanoclusters in the inner space that had high capability toward robust bending targeting a soft battery platform. The p-SiO_2 loadings in the flexible anodes reached to 1.62 mg/cm^2, which was comparable with commercial LIB anodes. Benefiting from the high interfacial stability and the well-interconnected skeleton of the N-CNFs, the anodes of p-SiO_2@N-CNF effectively tackled the issues of large volume expansion and unstable SEI of SiO_2 as anode materials and thus demonstrated a robust electrochemical operation of soft LIBs. In addition, we concluded that both the NP doping and the graphitic carbon layers embedded in the CNF matrix endowed the flexibility of the anode and performed as softness plasticizer to scatter the concentrated force, and thus avoid cracks on the overall structure. As a result of the hierarchical structure design strategy, the soft LIBs containing the flexible anodes exhibited high rate capability from 0.1–10 C and long-term stability over 1,000 cycles. More importantly, prepared by a simple procedure that could be broadly applied, this anode design strategy paves the way to the fabrication of high-performance silicon-based LIBs with robust durability.

Limitation of the Study

Although our preliminary results show that the anodes of p-SiO_2@N-CNF had promising performance for constructing flexible Li-batteries, if the following two technical risks can be addressed, the performance of such flexible anodes will be significantly enhanced. (1) During our preliminary research, we used small pieces of the free-standing membranes to assemble batteries, but when increasing the electrode area substantially (i.e., tens of square centimeters), the sheet resistance of anode might be much higher. (2) Main challenge in flexible batteries lies in maintaining the energy density while enhancing the flexibility; however, in this study, we only tested the electrochemical performance of the flexible batteries under certain bending degrees (0 and 90°).

METHODS

All methods can be found in the accompanying Transparent Methods supplemental file.

SUPPLEMENTAL INFORMATION

Supplemental Information can be found online at https://doi.org/10.1016/j.isci.2019.05.023.

ACKNOWLEDGMENTS

This work is supported by the Key Laboratory of Textile Science & Technology (Donghua University), Ministry of Education (2232018G-01); the National Natural Science Foundation of China (No. 51702047); the National Key R&D Program of China (No. SQ2018YFC200227); the State Administration of Science, Technology and Industry for National Defence, PRC (JCKY2018203c035); and the Young Elite Scientists Sponsorship Program by CAST (No. 2018QNRC001).

AUTHOR CONTRIBUTIONS

J.Yan and B.D. conceived and designed the project, analyzed the experimental data. A.A.A., Y.Z., K.D., and X.W. conducted the synthesis experiments and material characterizations. J.Yan and A.A.A. conducted battery tests and analysis. A.A.A. and J.Yan wrote this paper, and all authors contributed to discussing and revising the paper.

DECLARATION OF INTERESTS

The authors declare no competing interests.

Received: February 20, 2019
Revised: April 7, 2019
Accepted: May 16, 2019
Published: June 28, 2019

REFERENCES

An, W., Fu, J., Su, J., Wang, L., Peng, X., Wu, K., Chen, Q., Bi, Y., Gao, B., and Zhang, X. (2017). Mesoporous hollow nanospheres consisting of carbon coated silica nanoparticles for robust lithium-ion battery anodes. J. Power Sources *345*, 227–236.

Aricò, A.S., Bruce, P., Scrosati, B., Tarascon, J.-M., and van Schalkwijk, W. (2005). Nanostructured materials for advanced energy conversion and storage devices. Nat. Mater. *4*, 366.

Beaulieu, L., Eberman, K., Turner, R., Krause, L., and Dahn, J. (2001). Colossal reversible volume changes in lithium alloys. Electrochem. Solid State Lett. *4*, A137–A140.

Chang, J., Shang, J., Sun, Y., Ono, L.K., Wang, D., Ma, Z., Huang, Q., Chen, D., Liu, G., and Cui, Y. (2018). Flexible and stable high-energy lithium-sulfur full batteries with only 100% oversized lithium. Nat. Commun. *9*, 4480.

Chang, W.-S., Park, C.-M., Kim, J.-H., Kim, Y.-U., Jeong, G., and Sohn, H.-J. (2012). Quartz (SiO 2): a new energy storage anode material for Li-ion batteries. Energy Environ. Sci. *5*, 6895–6899.

Chen, T., Wu, J., Zhang, Q., and Su, X. (2017). Recent advancement of SiOx based anodes for lithium-ion batteries. J. Power Sources *363*, 126–144.

Deng, Y., Xie, Y., Zou, K., and Ji, X. (2016). Review on recent advances in nitrogen-doped carbons: preparations and applications in supercapacitors. J. Mater. Chem. A *4*, 1144–1173.

Dirican, M., Yildiz, O., Lu, Y., Fang, X., Jiang, H., Kizil, H., and Zhang, X. (2015). Flexible binder-free silicon/silica/carbon nanofiber composites as anode for lithium–ion batteries. Electrochim. Acta *169*, 52–60.

Etacheri, V., Marom, R., Elazari, R., Salitra, G., and Aurbach, D. (2011). Challenges in the development of advanced Li-ion batteries: a review. Energ Environ. Sci. *4*, 3243–3262.

Ge, J., Qu, Y., Cao, L., Wang, F., Dou, L., Yu, J., and Ding, B. (2016). Polybenzoxazine-based highly porous carbon nanofibrous membranes hybridized by tin oxide nanoclusters: durable mechanical elasticity and capacitive performance. J. Mater. Chem. A *4*, 7795–7804.

Goodenough, J.B., and Kim, Y. (2009). Challenges for rechargeable Li batteries. Chem. Mater. *22*, 587–603.

Goriparti, S., Miele, E., De Angelis, F., Di Fabrizio, E., Zaccaria, R.P., and Capiglia, C. (2014). Review on recent progress of nanostructured anode materials for Li-ion batteries. J. Power Sources *257*, 421–443.

Guo, B., Shu, J., Wang, Z., Yang, H., Shi, L., Liu, Y., and Chen, L. (2008). Electrochemical reduction of nano-SiO2 in hard carbon as anode material for lithium ion batteries. Electrochem. Commun. *10*, 1876–1878.

Hu, Q., Wang, X., and Wang, Z. (2013). Preparation of graphitic carbon nanofibres by in situ catalytic graphitisation of phenolic resins. Ceram. Int. *39*, 8487–8492.

Hu, Y., and Sun, X. (2014). Flexible rechargeable lithium ion batteries: advances and challenges in materials and process technologies. J. Mater. Chem. A *2*, 10712–10738.

Jang, S.-M., Miyawaki, J., Tsuji, M., Mochida, I., and Yoon, S.-H. (2009). The preparation of a novel Si–CNF composite as an effective anodic material for lithium–ion batteries. Carbon *47*, 3383–3391.

Jeschull, F., Brandell, D., Edström, K., and Lacey, M.J. (2015). A stable graphite negative electrode for the lithium–sulfur battery. Chem. Commun. *51*, 17100–17103.

Ji, H., Ma, C., Ding, J., Yang, J., Yang, G., Chao, Y., and Yang, Y. (2019). Complementary stabilization by core/sheath carbon nanofibers/spongy carbon on submicron tin oxide particles as anode for lithium-ion batteries. J. Power Sources *413*, 42–49.

Kim, H., Lim, K., Yoon, G., Park, J.H., Ku, K., Lim, H.D., Sung, Y.E., and Kang, K. (2017). Exploiting lithium–ether co-intercalation in graphite for high-power lithium-ion batteries. Adv. Energy Mater. *7*, 1700418.

Kim, Y.-K., Moon, J.-W., Lee, J.-G., Baek, Y.-K., and Hong, S.-H. (2014). Porous carbon-coated silica macroparticles as anode materials for

lithium ion batteries: effect of boric acid. J. Power Sources *272*, 689–695.

Li, W., Li, M., Adair, K.R., Sun, X., and Yu, Y. (2017). Carbon nanofiber-based nanostructures for lithium-ion and sodium-ion batteries. J. Mater. Chem. A *5*, 13882–13906.

Li, X., Dhanabalan, A., Meng, X., Gu, L., Sun, X., and Wang, C. (2012). Nanoporous tree-like SiO2 films fabricated by sol–gel assisted electrostatic spray deposition. Microporous Mesoporous Mater. *151*, 488–494.

Li, Z., Zhang, J., Shu, J., Chen, J., Gong, C., Guo, J., Yu, L., and Zhang, J. (2018). Carbon nanofibers with highly dispersed tin and tin antimonide nanoparticles: preparation via electrospinning and application as the anode materials for lithium-ion batteries. J. Power Sources *381*, 1–7.

Liu, N., Huo, K., McDowell, M.T., Zhao, J., and Cui, Y. (2013). Rice husks as a sustainable source of nanostructured silicon for high performance Li-ion battery anodes. Sci. Rep. *3*, 1919.

Manthiram, A. (2011). Materials challenges and opportunities of lithium ion batteries. J. Phys. Chem. Lett. *2*, 176–184.

Meng, J., Cao, Y., Suo, Y., Liu, Y., Zhang, J., and Zheng, X. (2015). Facile fabrication of 3D SiO2@ graphene aerogel composites as anode material for lithium ion batteries. Electrochim. Acta *176*, 1001–1009.

Obrovac, M., and Christensen, L. (2004). Structural changes in silicon anodes during lithium insertion/extraction. Electrochem. Solid State Lett. *7*, A93–A96.

Obrovac, M., Christensen, L., Le, D.B., and Dahn, J.R. (2007). Alloy design for lithium-ion battery anodes. J. Electrochem. Soc. *154*, A849–A855.

Pan, H., Yang, J., Wang, S., Xiong, Z., Cai, W., and Liu, J. (2015). Facile fabrication of porous carbon nanofibers by electrospun PAN/dimethyl sulfone for capacitive deionization. J. Mater. Chem. A *3*, 13827–13834.

Panomsuwan, G., Saito, N., and Ishizaki, T. (2015). Nitrogen-doped carbon nanoparticles derived from acrylonitrile plasma for electrochemical oxygen reduction. Phys. Chem. Chem. Phys. *17*, 6227–6232.

Qu, E., Chen, T., Xiao, Q., Lei, G., and Li, Z. (2018). Freestanding silicon/carbon nanofibers composite membrane as a flexible anode for Li-Ion battery. J. Power Sources *403*, 103–108.

Rao, J., Liu, N., Zhang, Z., Su, J., Li, L., Xiong, L., and Gao, Y. (2018). All-fiber-based quasi-solid-state lithium-ion battery towards wearable electronic devices with outstanding flexibility and self-healing ability. Nano Energy *51*, 425–433.

Sasidharan, M., Liu, D., Gunawardhana, N., Yoshio, M., and Nakashima, K. (2011). Synthesis, characterization and application for lithium-ion rechargeable batteries of hollow silica nanospheres. J. Mater. Chem. *21*, 13881–13888.

Sui, G., Zhao, Y., Zhang, Q., and Fu, Q. (2016). Enhanced mechanical properties of olefin block copolymer by adding a quaternary ammonium salt functionalized graphene oxide. RSC Adv. *6*, 54785–54792.

Sun, Q., Zhang, B., and Fu, Z.-W. (2008). Lithium electrochemistry of SiO2 thin film electrode for lithium-ion batteries. Appl. Surf. Sci. *254*, 3774–3779.

Tan, J., Han, Y., He, L., Dong, Y., Xu, X., Liu, D., Yan, H., Yu, Q., Huang, C., and Mai, L. (2017). In situ nitrogen-doped mesoporous carbon nanofibers as flexible freestanding electrodes for high-performance supercapacitors. J. Mater. Chem. A *5*, 23620–23627.

Tu, J., Yuan, Y., Zhan, P., Jiao, H., Wang, X., Zhu, H., and Jiao, S. (2014). Straightforward approach toward SiO2 nanospheres and their superior lithium storage performance. J. Phys. Chem. C *118*, 7357–7362.

Wang, S., Liu, N., Su, J., Li, L., Long, F., Zou, Z., Jiang, X., and Gao, Y. (2017). Highly stretchable and self-healable supercapacitor with reduced graphene oxide based fiber springs. ACS Nano *11*, 2066–2074.

Wang, T., Shi, S., Li, Y., Zhao, M., Chang, X., Wu, D., Wang, H., Peng, L., Wang, P., and Yang, G. (2016a). Study of microstructure change of carbon nanofibers as binder-free anode for high-performance lithium-ion batteries. ACS Appl. Mater. Interfaces *8*, 33091–33101.

Wang, Y., Xie, K., Guo, X., Zhou, W., Song, G., and Cheng, S. (2016b). Mesoporous silica nanoparticles as high performance anode materials for lithium-ion batteries. New J. Chem. *40*, 8202–8205.

Winter, M., Barnett, B., and Xu, K. (2018). Before Li ion batteries. Chem. Rev. *118*, 11433–11456.

Wu, H., Chan, G., Choi, J.W., Ryu, I., Yao, Y., McDowell, M.T., Lee, S.W., Jackson, A., Yang, Y., and Hu, L. (2012). Stable cycling of double-walled silicon nanotube battery anodes through solid–electrolyte interphase control. Nat. Nanotechnol. *7*, 310.

Wu, J., Pan, Z., Zhang, Y., Wang, B., and Peng, H. (2018). The recent progress of nitrogen-doped carbon nanomaterials for electrochemical batteries. J. Mater. Chem. A *6*, 12932–12944.

Yan, N., Wang, F., Zhong, H., Li, Y., Wang, Y., Hu, L., and Chen, Q. (2013). Hollow porous SiO 2 nanocubes towards high-performance anodes for lithium-ion batteries. Sci. Rep. *3*, 1568.

Yang, X., Huang, H., Li, Z., Zhong, M., Zhang, G., and Wu, D. (2014). Preparation and lithium-storage performance of carbon/silica composite with a unique porous bicontinuous nanostructure. Carbon *77*, 275–280.

Ye, G., Zhu, X., Chen, S., Li, D., Yin, Y., Lu, Y., Komarneni, S., and Yang, D. (2017). Nanoscale engineering of nitrogen-doped carbon nanofiber aerogels for enhanced lithium ion storage. J. Mater. Chem. A *5*, 8247–8254.

Yuan, Z., Zhao, N., Shi, C., Liu, E., He, C., and He, F. (2016). Synthesis of SiO2/3D porous carbon composite as anode material with enhanced lithium storage performance. Chem. Phys. Lett. *651*, 19–23.

Yue, Y., Yang, Z., Liu, N., Liu, W., Zhang, H., Ma, Y., Yang, C., Su, J., Li, L., and Long, F. (2016). A flexible integrated system containing a microsupercapacitor, a photodetector, and a wireless charging coil. ACS Nano *10*, 11249–11257.

Zhou, X., Cao, A.-M., Wan, L.-J., and Guo, Y.-G. (2012). Spin-coated silicon nanoparticle/graphene electrode as a binder-free anode for high-performance lithium-ion batteries. Nano Res. *5*, 845–853.

ISCI, Volume *16*

Supplemental Information

Self-Assembled Porous-Silica within N-Doped Carbon Nanofibers as Ultra-flexible Anodes for Soft Lithium Batteries

Ahmed A. Aboalhassan, Jianhua Yan, Yun Zhao, Keqi Dong, Xiao Wang, Jianyong Yu, and Bin Ding

Supplementary Figures

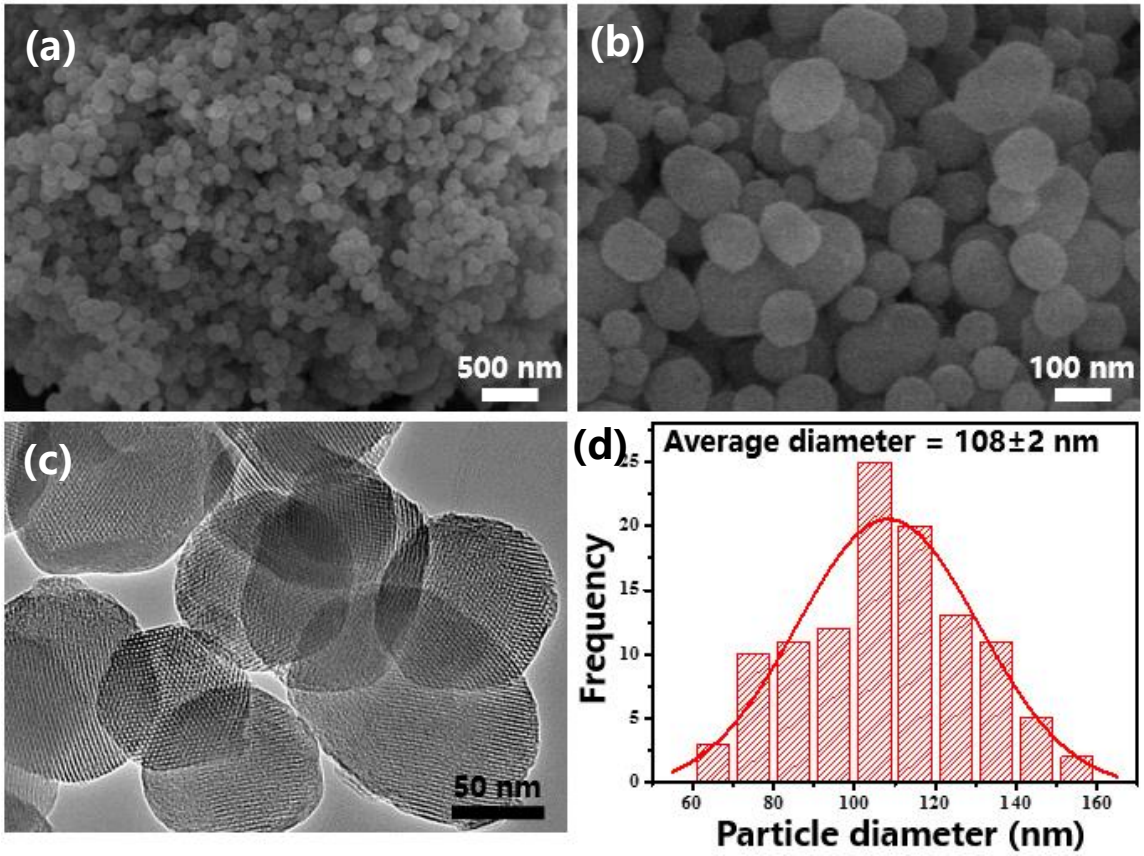

Figure S1. Morphology and particle size distribution of the synthesized p-SiO_2 NPs, related to Figure 1(b).

(**a-c**) SEM and TEM images of the synthesized p-SiO_2 NPs in different magnifications and, (**d**) the particle diameter distribution histogram. The particles had well-distributed nano-pores and uniform particle sizes. The average particle size was calculated as 108 nm.

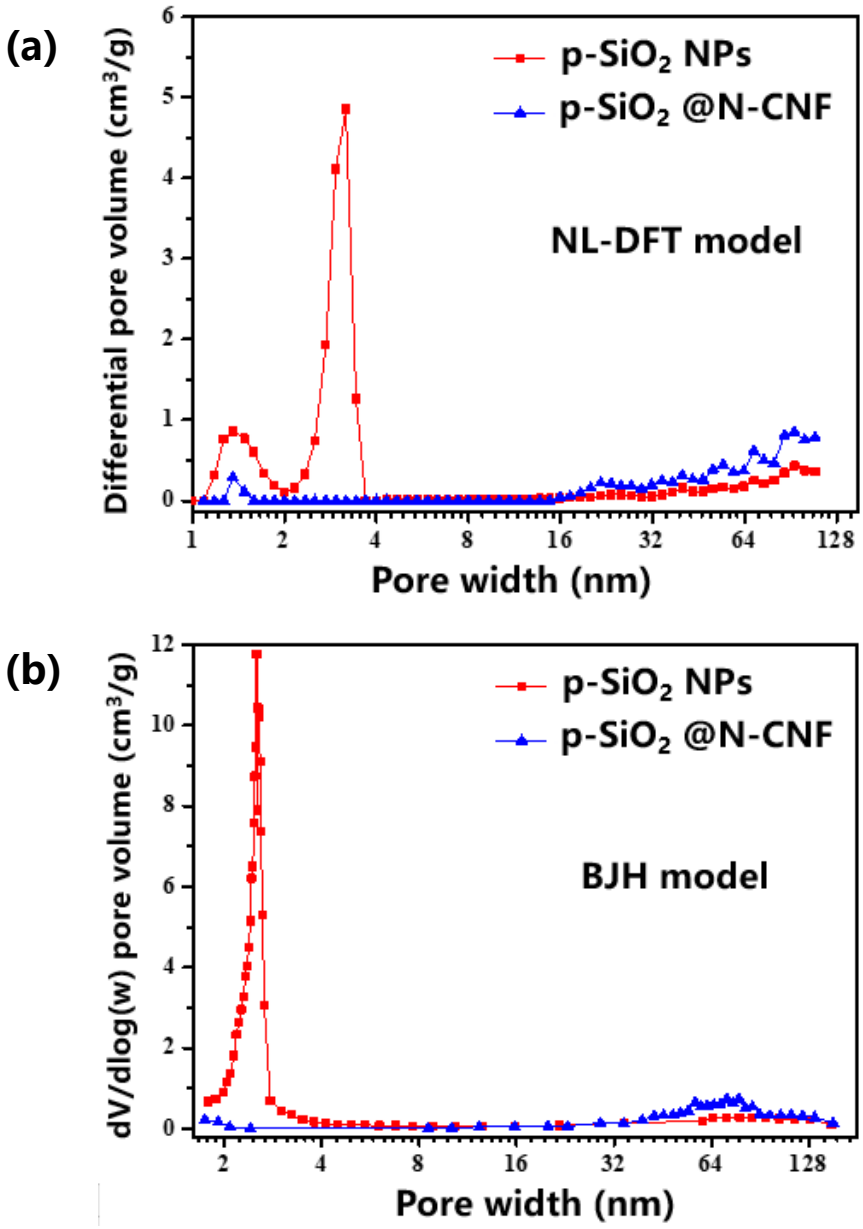

Figure S2. Pore size distribution of the synthesized p-SiO_2 NPs and p-SiO_2 @N-CNFs, related to Figure 2(b) and Table S1.

Testing curves of pore size distributions and pore volumes in the synthesized p-SiO_2 NPs and p-SiO_2 @N-CNFs. Analyses were based on the method of 2-D nonlocal density functional theory (2D-NLDFT). Two models of (**a**) NLDFT and (**b**) BJH were used to calculate the pore volumes and the total pore volumes, as summarized in Table S1.

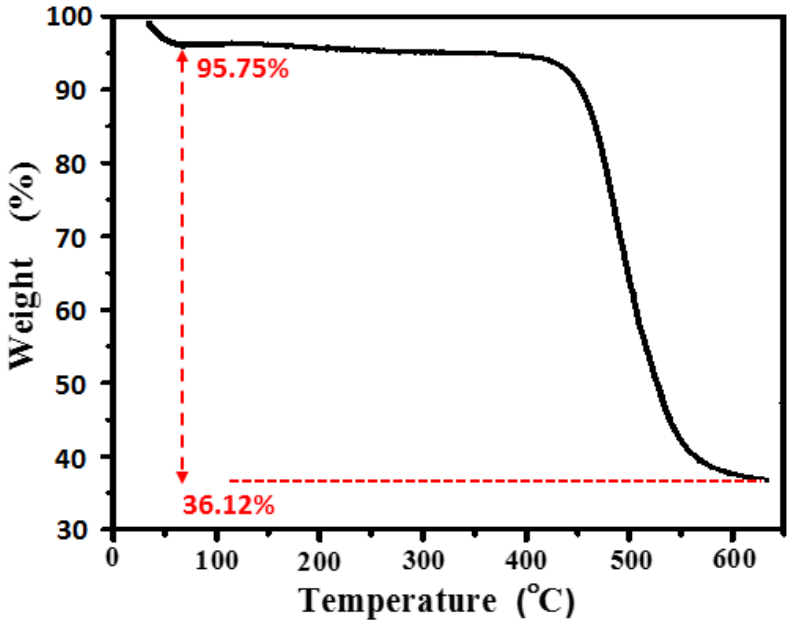

Figure S3. TG analysis of the p-SiO_2@N-CNF in air atmosphere, related to Figure 3.

The test started from room temperature to 650 ℃ at a heating rate of 5 ℃ min^{-1}. The content of SiO_2 was calculated as follows wt.%= 36.12/95.75=37.7%.

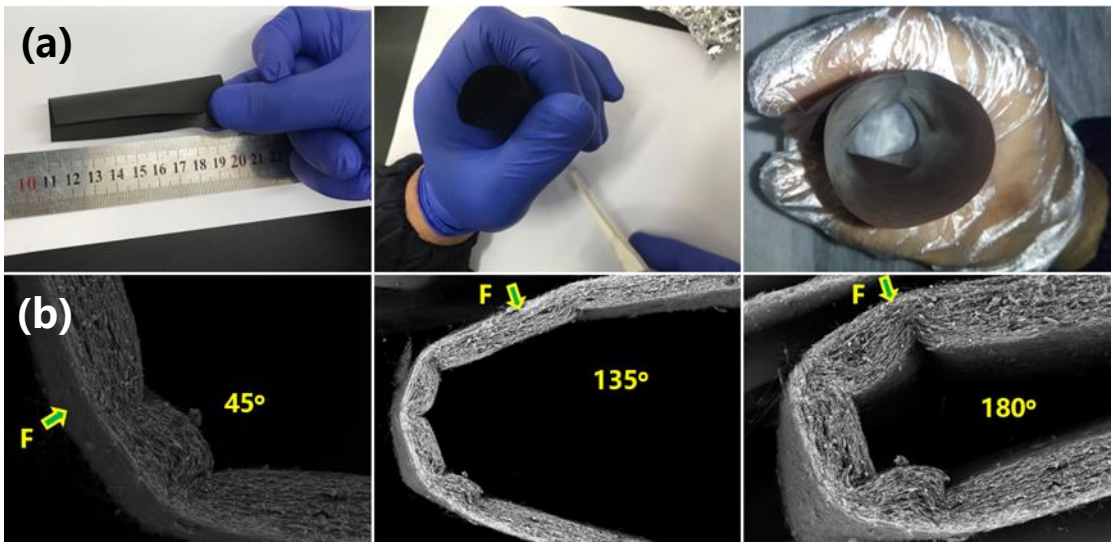

Figure S4. p-SiO_2@N-CNF under various deforming states, related to Figure 3.

(a) Digital photos of the anodes of p-SiO_2@N-CNF under various bending, rolling and deforming states. **(b)** The corresponding cross-sectional SEM images with diverse angles of the nanofibrous membranes. There were not obvious cracks after deforming.

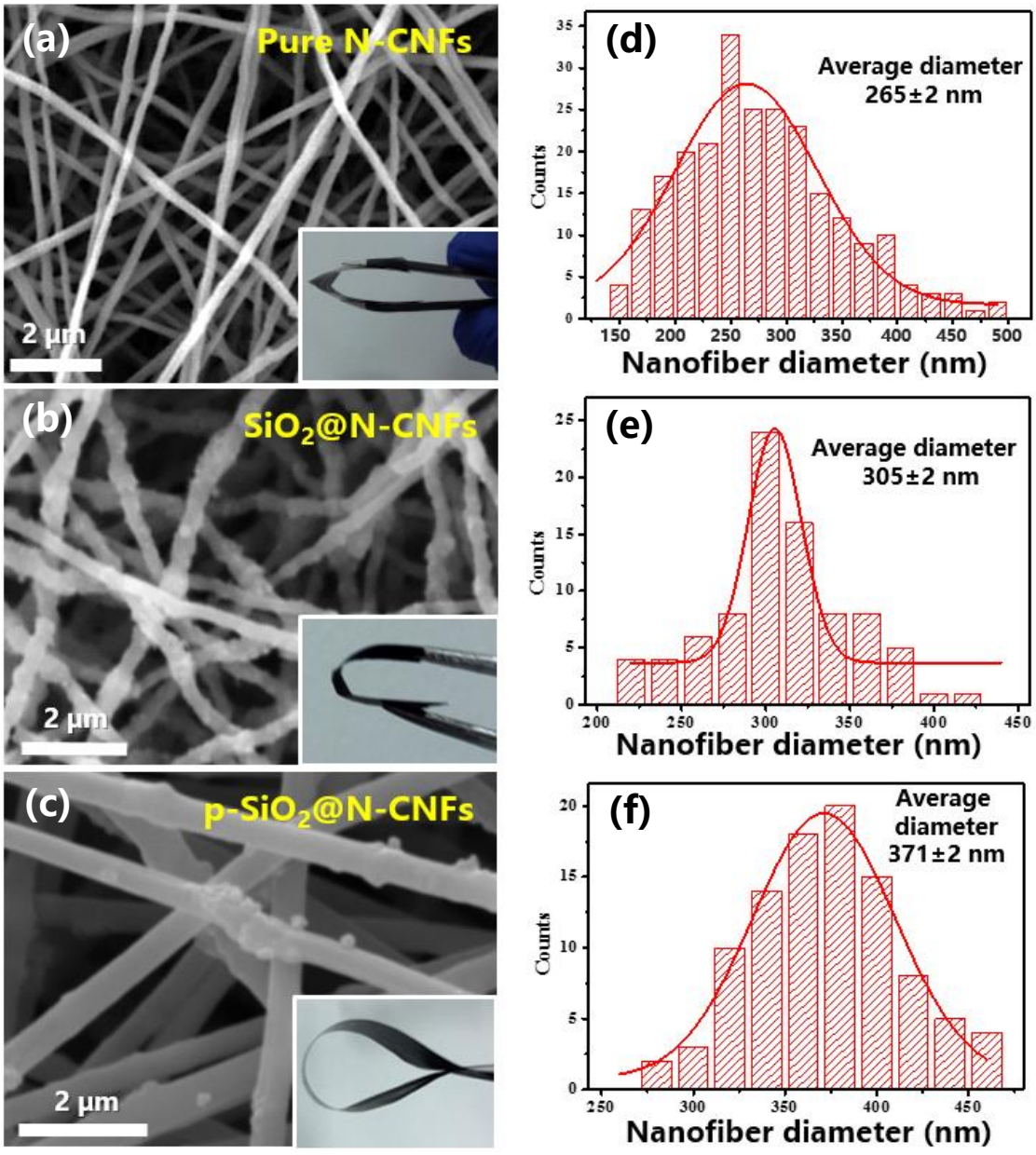

Figure S5. SEM images of the different anodes, related to the figure 3(a).

SEM images of **(a)** the pure CNFs, **(b)** the SiO_2@N-CNFs and **(c)** the p-SiO_2@N-CNFs with digital photo images under bending states; (**d-f**) statistical analysis of their corresponding NF diameter histograms.

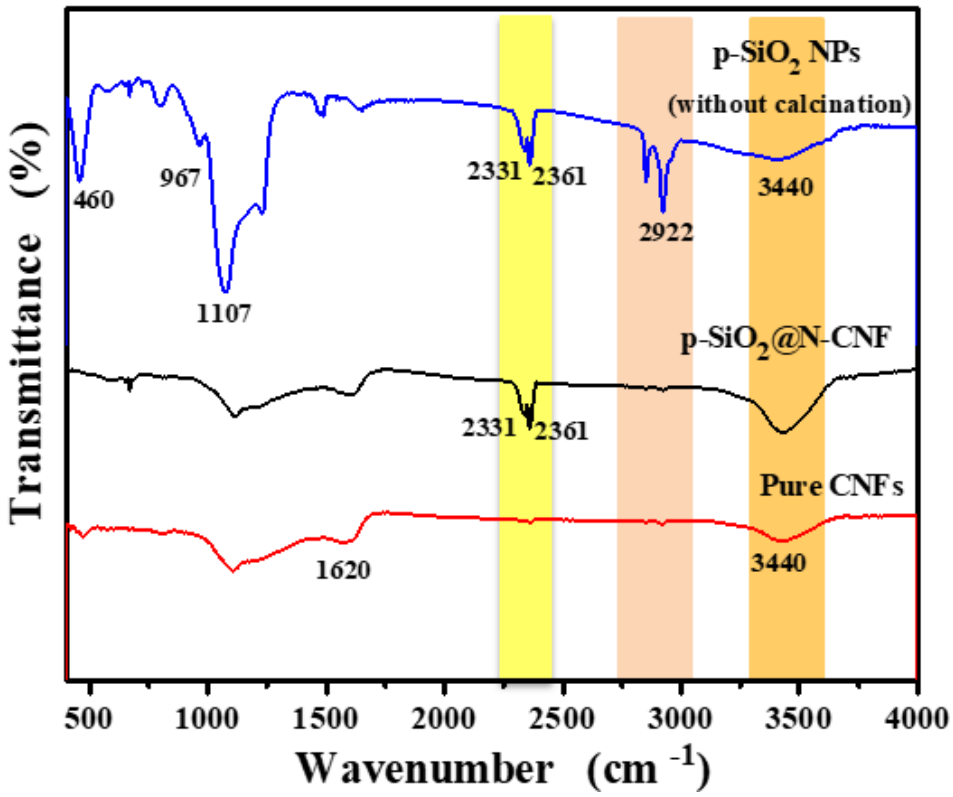

Figure S6. FTIR spectra of indicating the CTAB removal and p-SiO_2 loadings on the N-CNFs, related to Figure 3.

FTIR spectra of the p-SiO_2 NPs without calcination, p-SiO_2@N-CNF and the pure N-CNFs. The peaks at 460, 967, 1107 cm^{-1} were assigned for the Si-O rocking vibration, Si-O bond stretching and internal Si-O-Si stretching vibrations, respectively. The twin peaks at 2331, 2361 cm^{-1} were attributed to the presence of SiO_2 on the N-CNFs, which were not observed in the pure CNFs. For the pure N-CNFs, the obvious peak at 1620 cm^{-1} was attributed to C=C and C-O bonds, and the peak at 3440 cm^{-1} was assigned for the primary and/or the secondary N-H stretch and O-H stretch. It is worthy note that the disappearance of the absorption peak at 2922 cm^{-1} in p-SiO_2@N-CNF revealed that CTAB was completely removed (Hao et al., 2016; Jing et al., 2011).

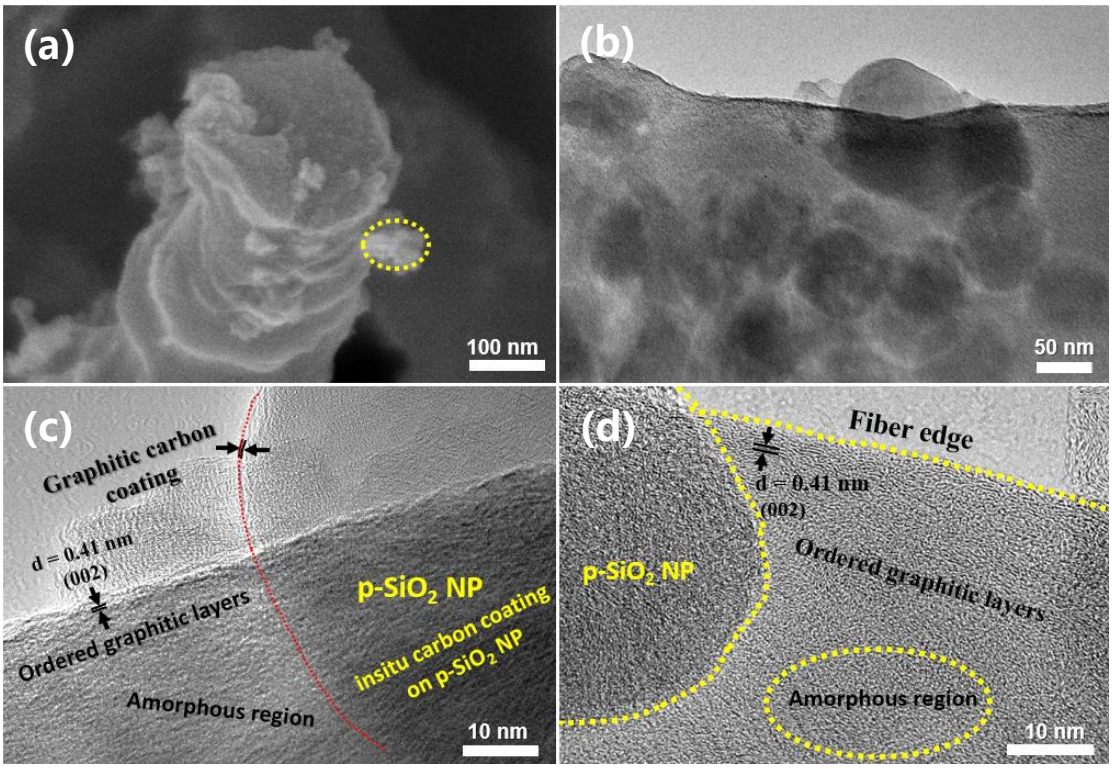

Figure S7. The cross-section morphology and TEM of the fabricated anodes, realted to Figure 3(e).

(a) The cross-section FE-SEM images of the SiO_2@N-CNF, in which most of the NPs located out of the NFs. (**b-d**) TEM images of the p-SiO_2@N-CNF to show the *in-situ* formed graphitic and amorphous carbon domains over p-SiO_2 NPs.

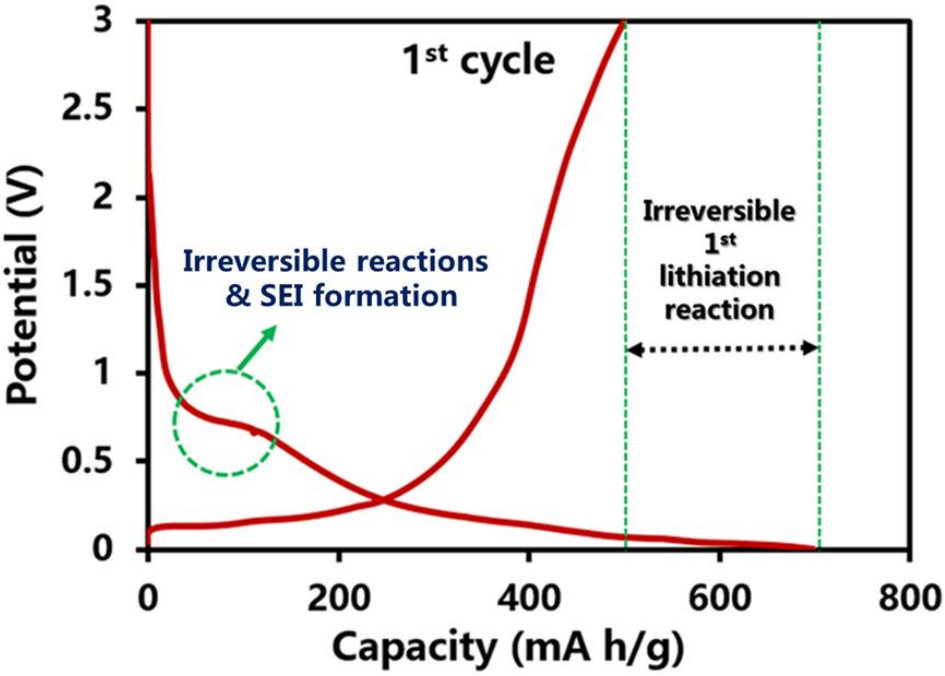

Figure S8. The 1st voltage profiles of the p-SiO_2@N-CNF, realted to Figure 5(c).

The low initial Coulombic Efficiency was probably caused by the irreversible reactions between Li-ions and SiO_2 to form silicon as follows (Guo et al., 2008):

1st Lithiation reactions with different proportions (irreversible reactions)

$$SiO_2 + 4Li^+ + 4e^- \longrightarrow 2\,Li_2O + Si$$

Or $$2\,SiO_2 + 4Li^+ + 4e^- \longrightarrow Li_4SiO_4 + Si$$

While; from the 2nd cycle, the lithiation reactions are as follows

$$Si + x\,Li^+ + x\,e^- \longleftrightarrow Li_xSi$$

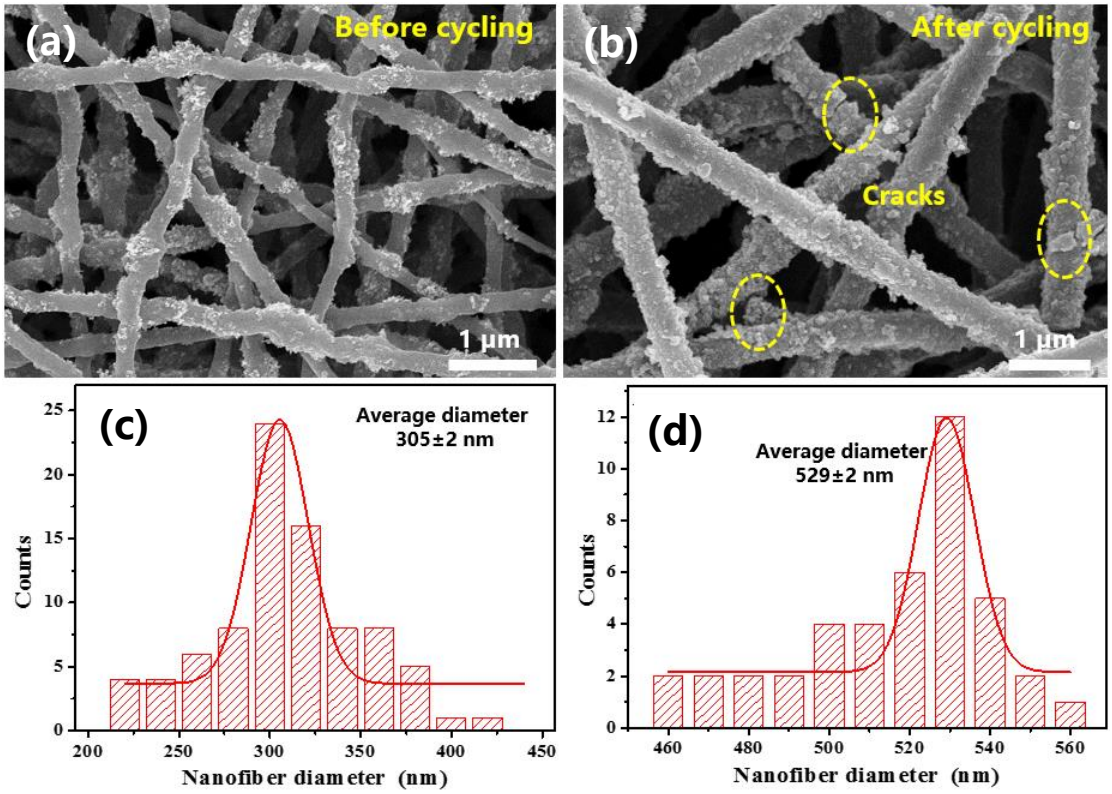

Figure S9. Postmortem analysis of the anodes of SiO_2@N-CNF, realted to Figure 5(c).

The FE-SEM images of the anodes of SiO_2@N-CNF (**a**) before and (**b**) after 500 cycles at 1 C; (**c, d**) the corresponding NF diameter histograms. The commercial SiO_2 NPs caused a large NF diameter change from 305 nm to 529 nm, corresponding to 1.73 times of expansion.

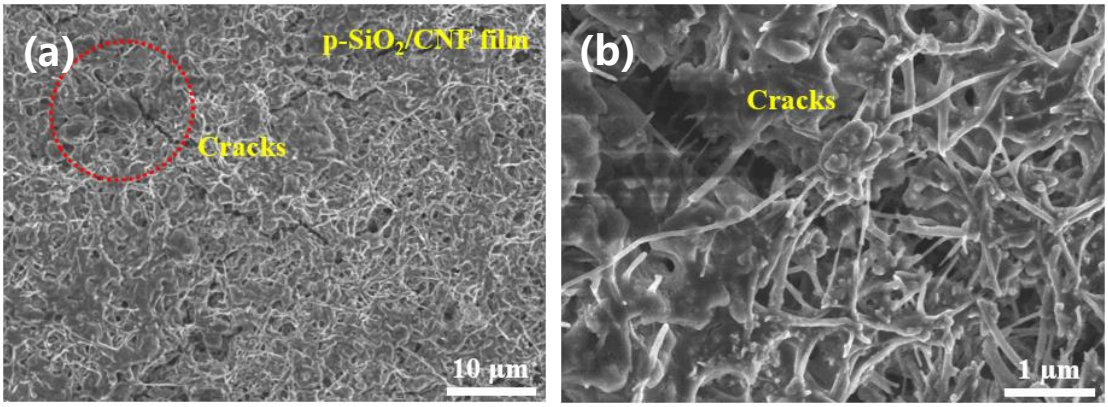

Figure S10. Postmortem analysis of the anodes that were fabricated by physically mixing p-SiO_2 NPs with N-CNF, realted to Figure 5(c).

Characterizations of the anodes comprising 38 wt.% of p-SiO_2, 52 wt.% of CNFs and 10 wt.% percent of PVDF binder. After 500 cycles, multiple large cracks were formed on the surface of the anodes due to volume changes of SiO_2 during the lithiation and delithiation processes.

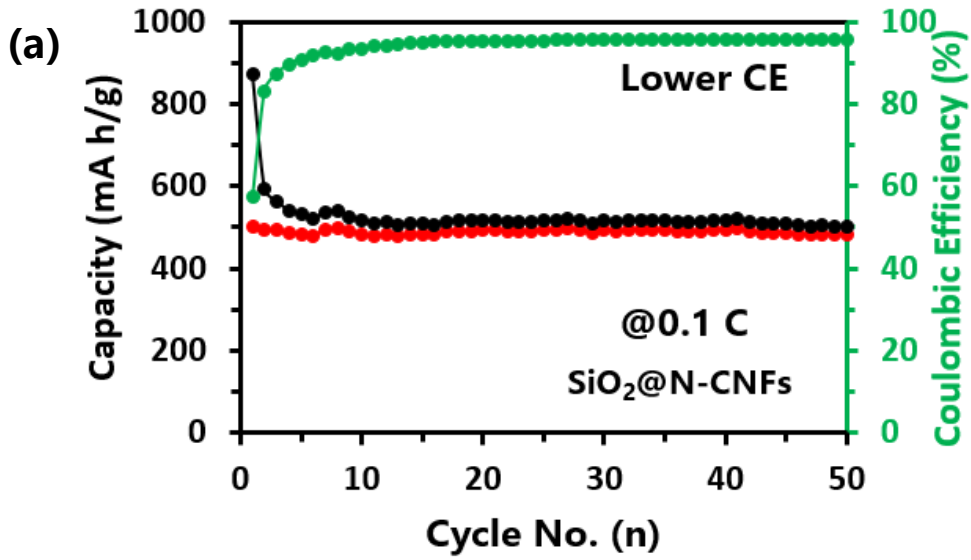

Figure S11. Performance of the anodes of SiO_2@N-CNF, related to Figure 5.

Cycling performance of batteries (Li/SiO_2@N-CNF) at **(a)** 0.1 C and **(b)** 1 C. The batteries had a fast capacity fade rate and a low Coulombic efficiency.

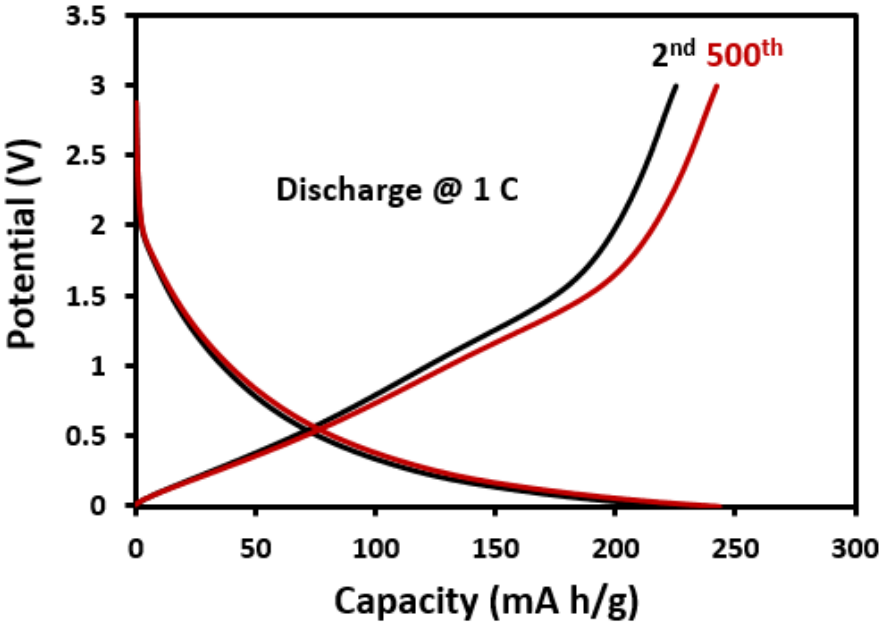

Figure S12. Performance of the anodes of p-SiO_2@N-CNF that were assembled in soft batteries, related to Figure 5(e).

The 2nd and the 500th Galvanostatic charge-discharge profiles of the composite anodes of p-SiO_2@N-CNF under a bending state of 90 degrees at a discharge rate of 1 C.

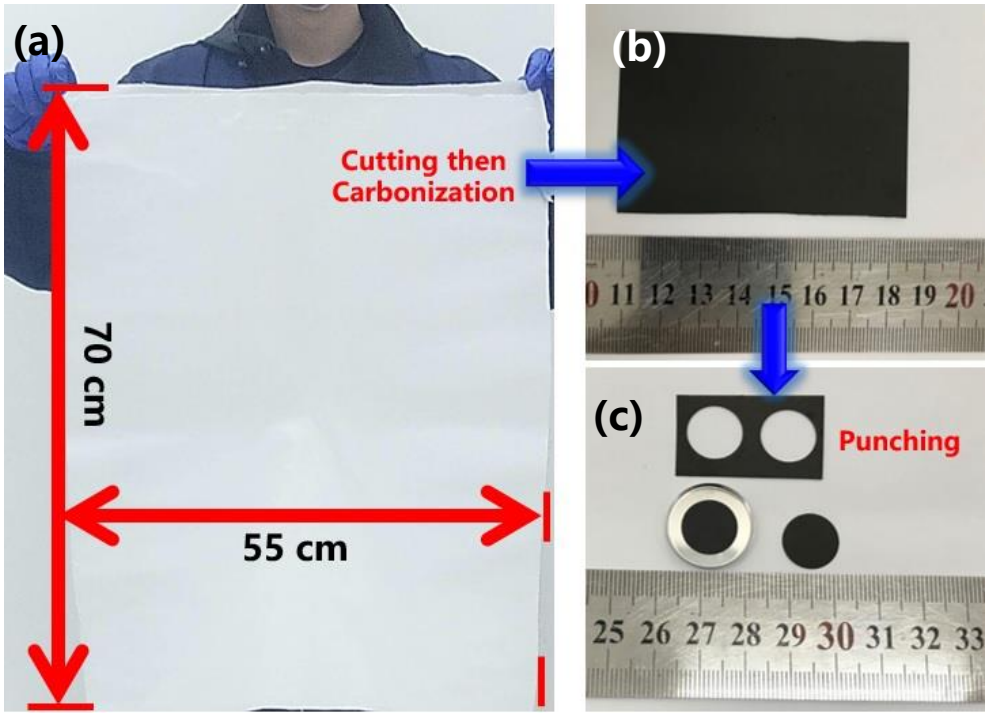

Figure S13. Scalable fabrication of the membranes, related to Figure 5.

(a) The digital photo of the as-spun membrane with a size of 70 cm x 55 cm. Before heating these membranes to carbon, we cut the membranes into small pieces due to the limited furnace space in our lab. (**b**) The divided membrane of p-SiO_2@N-CNF and (**c**) the corresponding punched free-standing anodes.

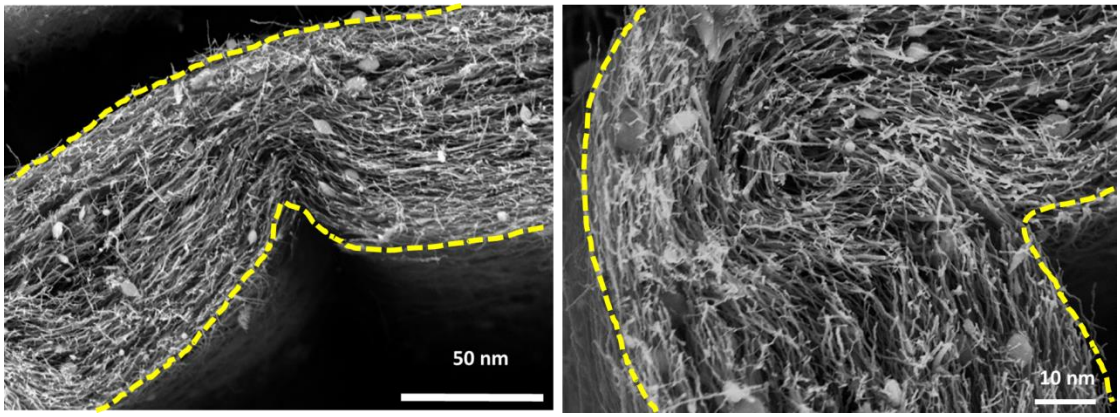

Figure S14. Robust flexibility of the anodes of p-SiO_2 @N-CNF, related to Figure 5.

SEM images of the composite anode of p-SiO_2 @N-CNF under applied bending forces with two different magnifications

Supplementary Table

Table S1. The pore texture parameters of SiO_2 NPs and p-SiO_2 @N-CNF, related to Figure 2(b).

Samples	**(V_t) (cm^3/g)**	**(V_{meso}) (cm^3/g)**	**(PVF_{meso}) (%)**
p-SiO_2 NPs	0.8678	0.4887	56.31
p-SiO_2@N-CNF	0.3457	0.106	30.66

(V_t): the total pore volume

(V_{meso}): the Mesoporous pore volume,

(PVF_{meso}): the fraction ratio of the mesopore volume to the total pore volume;

calculation based on Barret-Joyner-Halenda (BJH) model(Ge et al., 2016).

Transparent Methods

Materials

Polyacrylonitrile (PAN, Mw = 90000) was purchased from Spectrum Chemicals & Laboratory Products Co., Ltd, USA. N,N-Dimethyl formamide (DMF), absolute ethanol (EtOH, 99.5%), hydrochloric acid (HCl, 37%) and Sodium Hydroxide (NaOH) were obtained from the Shanghai Chemical Reagents Co., Ltd, China. Tetraethoxysilane (TEOS) and cetyltrimethyl ammonium bromide (CTAB) were supplied by Macklin Biochemical Co., Ltd., China. Commercial SiO_2 NPs (particles diameter ~100 nm) was provided from Aladdin Chemistry Co. Ltd, China. Deionized (DI) water produced by a Water Purification System (UPT-11-20T) was used during this work. All chemicals possess an analytical grade and were used without further purification.

Synthesis of p-SiO_2 NPs

Typically, as described previously, 1 mg of CTAB was stirred in 480 ml of DI H_2O and then 3.5 ml of 2 molar solution of NaOH were added and stirred vigorously at 80 ℃. Subsequently, TEOS (5 ml) was drop-wise added to the mixture and the

resultant was then kept under stirring for 2 hours. Subsequently, a white precipitate was separated via the vacuum filtration. Finally, a white precipitate of p-SiO_2 NPs containing CTAB template was obtained and then dried at 100 ℃ overnight under vacuum. For comparative analysis, to get the non-containing CTAB porous particles, the obtained dried white precipitate was washed for several times with EtOH and DI-H_2O alternatively, and a step of calcination to remove the CTAB template was done in a muffle furnace at 550 ℃ for 5 hours in air atmosphere.

Fabrication of self-interlocked p-SiO_2@N-CNF membranes

An appropriate amount of p-SiO_2 NPs was dispersed homogenously in Dimethyl formamide (DMF) for 2 h by using a powerful ultrasonic bath. Next, PAN powder (10 wt %) was added to the suspensions and was stirred for 8 hours and then was ultra-sonicated for 2 hours at room temperature. The electrospinning process was then carried out with a rate of 1.2 mL/h, a voltage of 25 kV and a distance of 20 cm between the needle head and the rotating collector. The temperature and humidity in the electrospinning chamber were controlled at 25±5 ℃ and 50±5%, respectively. The as-spun PAN NFs were dried at 70 ℃ for 1 hour under vacuum to completely remove the remaining DMF. The films were then thermally treated at 280 ℃ for 2 hours with air cycling to remove CTAB while simultaneously pre-oxidizing PAN. Lastly, the films were annealed under high purity nitrogen (99.999%) at 800 ℃ for 2 hours. Similarly, the pure CNFs and commercial SiO_2@N-CNF were prepared with the same procedures.

Material Characterizations

Morphology and element distribution of the samples were checked by SEM (S-4800) and TEM (JEM-2100F), while crystallographic structures were tested by Bruker XRD (with Cu Kα, λ=1.5406 Å) and Raman (inVia-Reflex). The specific surface areas, the mesopore sizes and the pore volumes were examined by an automatic adsorption system analyzer (ASAP 2020, Micromeritics Co., USA) with both Brunauer-Emmett-Teller (BET) model and Barrett-Joynes-Halenda (BJH) model. Moreover, bonding spectrum in the NFs was tested by FTIR (Nicolet iS8). X-ray

photoelectron spectroscopy (XPS) was tested in a vacuumed chamber using (X-ray ThermoFischer, ESCALAB 250 Xi) with a monochromatic source Al-Kα (1486.6 eV). SiO_2 contents were determined by TGA (SDT Q600) heated from room temperature to 650 ℃ with a ramp rate of 5 ℃ min^{-1}. The softness of the NF membranes was assessed by a softness tester (RRY-1000) according to the standard of ASTM D 2923-06. The tensile mechanical properties of the NF membranes were measured by a tensile tester (XQ-1A) according to the international standard (ISO 1798:2008).

Soft battery assembly and electrochemical measurements

CR2025-type coin cells were assembled with the ring Li-foils (thickness of 20 μm and a diameter of 1.65 cm) or $LiFePO_4$ (containing 80 wt. % of $LiFePO_4$, 10 wt. % of PVDF and 10 wt. % of carbon black) as counterpart electrodes and Cellgard 2400 microporous membranes as separator. Soft batteries with a transparent PET (as battery cases) were also assembled. In both types of batteries, 1M $LiPF_6$ in ethylene carbonate, diethyl carbonate and ethyl methyl carbonate (EC: DEC: EMC = 1: 1: 1 v/v) was used as an electrolyte. All the cells were assembled within an Ar-filled Mikrouna lab glove box. For post-mortem examinations, the batteries disassembled in the Ar-filled gloves box and the electrodes were saved in Ar-filled bottles before testing. Electrochemical measurements were performed galvanostatically for charging and discharging between 0 and 3.0 V at various current densities using LAND-CT2001A battery testing system. Cyclic voltamograms (CV) were conducted using an electrochemical workstation (Chenhua, CHI 660E, Shanghai) at a scan rate of 0.1 mV/s. Meanwhile, the electrochemical impedance spectroscopy (EIS) was carried out employing the same electrochemical workstation in a frequency range between 100 kHz and 100 m Hz at potentiostatic signal amplitude of 10 mV. All experiments were conducted at room temperature.

Supplementary References

Ge, J., Qu, Y., Cao, L., Wang, F., Dou, L., Yu, J., and Ding, B. (2016). Polybenzoxazine-based highly porous carbon nanofibrous membranes hybridized by tin oxide nanoclusters: durable mechanical elasticity and capacitive performance. J. Mater. Chem. A. 4, 7795-7804.

Guo, B., Shu, J., Wang, Z., Yang, H., Shi, L., Liu, Y., and Chen, L. (2008). Electrochemical reduction of nano-SiO2 in hard carbon as anode material for lithium ion batteries. Electrochem. Commun. 10, 1876-1878.

Hao, N., Chen, X., Jayawardana, K.W., Wu, B., Sundhoro, M., and Yan, M. (2016). Shape control of mesoporous silica nanomaterials templated with dual cationic surfactants and their antibacterial activities. Biomaterials Science 4, 87-91.

Jing, W., Zhao, H., He, J., Wang, C., and Jie, W. (2011). Nano-sized SiO x /C composite anode for lithium ion batteries. J. Power Sources. 196, 4811-4815.